Augmin deficiency in neural stem cells causes p53-dependent apoptosis and aborts brain development.

Ricardo Viais[1], Marcos Fariña-Mosquera[1,#], Marina Villamor-Payà[1,#], Sadanori Watanabe[2,#], Lluís Palenzuela[1], Cristina Lacasa[1], Jens Lüders[1,*]

Affiliations:

[1]Institute for Research in Biomedicine (IRB Barcelona), The Barcelona Institute of Science and Technology (BIST), 08028 Barcelona, Spain

[2]Division of Biological Science, Graduate School of Science, Nagoya University, Chikusa-ku, Nagoya 464-8602, Japan

[#] authors contributed equally

*Correspondence: jens.luders@irbbarcelona.org

Short title: Augmin is essential for brain development

Key words: augmin, spindle, mitosis, neural progenitor, brain development

Abstract

Microtubules that assemble the mitotic spindle are generated by centrosomal nucleation, chromatin-mediated nucleation, and nucleation from the surface of other microtubules mediated by the augmin complex. Impairment of centrosomal nucleation in apical progenitors of the developing mouse brain induces p53-dependent apoptosis and causes non-lethal microcephaly. Whether disruption of non-centrosomal nucleation has similar effects is unclear. Here we show, using mouse embryos, that conditional knockout of the augmin subunit *Haus6* in apical progenitors led to spindle defects and mitotic delay. This triggered massive apoptosis and abortion of brain development. Co-deletion of *Trp53* rescued cell death, but surviving progenitors failed to organize a pseudostratified epithelium, and brain development still failed. This could be explained by exacerbated mitotic errors and resulting chromosomal defects including increased DNA damage. Thus, in contrast to centrosomes, augmin is crucial for apical progenitor mitosis, and, even in the absence of p53, for progression of brain development.

Introduction

Spindle assembly crucially depends on microtubule nucleation by the γ-tubulin ring complex (γTuRC). During mitosis γTuRC generates microtubules through three different pathways: centrosomal nucleation, chromatin-mediated nucleation, and nucleation from the surface of other microtubules (Meunier and Vernos, 2015; Petry, 2016; Prosser and Pelletier, 2017). The latter mechanism is mediated by the augmin complex and has been referred to as a microtubule amplification mechanism (Goshima et al., 2008; Goshima and Kimura, 2010; Lawo et al., 2009; Uehara et al.,

2009). Augmin binds to the lattice of microtubules generated by the centrosome- and chromatin-dependent pathways and, through recruitment of γTuRC, promotes nucleation of additional microtubules that grow as branches from these sites (Alfaro-Aco et al., 2020; Kamasaki et al., 2013; Petry et al., 2013; Tariq et al., 2020). The existence of multiple nucleation pathways may provide some level of redundancy to spindle assembly, but concerted action by multiple nucleation mechanisms has also been described (Hayward et al., 2014; Prosser and Pelletier, 2017). While functional studies in *Xenopus* egg extract and cultured cell models have generated a wealth of information regarding the types of spindle defects that occur when specific nucleation pathways are compromised, how these defects impinge on cell fate and development remains poorly defined.

Gene mutations that cause functional or numerical centrosome aberrations are associated with primary microcephaly, a developmental disorder that results in reduced thickness of the cerebral cortex. Depletion of apical progenitors following abnormal mitoses has been identified as a pathogenic mechanism (Jayaraman et al., 2018; Marthiens and Basto, 2020; Nano and Basto, 2017). Apical progenitors of the developing cerebral cortex are highly polarized cells. Their cell bodies are positioned in the ventricular zone (VZ), while their apical and basal processes contact the ventricular surface and basal lamina, respectively (Arai and Taverna, 2017; Chenn et al., 1998; Chou et al., 2018). Prior to mitosis the nucleus migrates apically and mitotic chromosome segregation occurs near the apical surface. Early during cortical development apical progenitors divide symmetrically, expanding the progenitor pool. At later stages they switch to self-renewing asymmetric mitoses, producing a neuron or intermediate progenitor in each division. Centrosomal microtubules were proposed to be at the core of these fate decisions, by controlling the distribution of cell fate

determinants through correct positioning of the mitotic spindle (Homem et al., 2015; Taverna et al., 2014; Uzquiano et al., 2018). Recent work showed that progenitor fate is strongly impacted by mitotic duration. Mitotic delay results in more neurogenic divisions and an increased percentage of progenitors undergoing p53-dependent apoptosis, depleting the progenitor pool (Mitchell-Dick et al., 2020; Pilaz et al., 2016). Consistently, mitotic delay, premature differentiation and apoptosis have all been observed for centrosome defects in mouse models of primary microcephaly (Insolera et al., 2014; Lin et al., 2020; Marjanović et al., 2015; McIntyre et al., 2012; Novorol et al., 2013). Interestingly, in cases where it has been tested, such as *Cenpj*- or *Cep63*-deficient mice, the reduced cortical thickness was fully rescued by co-deletion of *Trp53*, identifying p53-dependent apoptotic cell death as main driver of microcephaly in these models (Insolera et al., 2014; Marjanović et al., 2015). Recently, it was shown that this response involves the USP28-53BP1-p53-p21-dependent mitotic surveillance pathway, which is triggered by prolonged mitosis resulting from centrosome loss (Phan et al., 2021). Depletion of progenitors by apoptosis may be less important in human microcephaly, where organoid models have revealed premature differentiation as main response (Gabriel et al., 2016; Lancaster et al., 2013).

The roles of chromatin-mediated nucleation and augmin-dependent amplification in this context are less clear. Mouse embryos deficient for *Tpx2*, a spindle assembly factor that functions in chromatin-mediated nucleation, abort development after a few rounds of highly abnormal mitotic divisions (Aguirre-Portolés et al., 2012). Similar observations were made for mouse embryos lacking expression of the augmin subunit *Haus6* (Watanabe et al., 2016). However, since early mouse

development occurs in the absence of centrosomes (Gueth-Hallonet et al., 1993), the embryos in the above studies lacked two of the three mitotic nucleation pathways.

Early functional studies by augmin knockdown in cell lines described mitotic defects that ranged from relatively mild for *Drosophila* cells (Goshima et al., 2008; Meireles et al., 2009) to more severe for human cells (Lawo et al., 2009), suggesting cell type- or organism-specific differences. Consistent with this, the knockout of augmin in *Aspergillus* has no obvious phenotype (Edzuka et al., 2014), *Drosophila* augmin mutants are viable with mild mitotic defects observed in only some cell types (Meireles et al., 2009; Wainman et al., 2009), and a zebrafish mutant is also viable but displays defects in the expansion and maintenance of the hematopoietic stem cell pool (Du et al., 2011). A more recent inducible knockout of the augmin subunit *HAUS8* in non-transformed human RPE1 cells caused mild spindle defects before cells underwent p53-dependent G1 arrest, but co-deletion of *Trp53* exacerbated the mitotic phenotype (McKinley and Cheeseman, 2017). This response may involve the USP28-53BP1-p53-p21-dependent mitotic surveillance pathway, which is triggered by centrosome loss or prolonged mitosis (Fong et al., 2016; Lambrus et al., 2016; Meitinger et al., 2016), but this was not directly tested.

To uncover the specific role of augmin-mediated microtubule amplification in mitotic spindle assembly and cell fate determination, we sought to study augmin deficiency in centrosome-containing cells *in vivo*. To this end we conditionally knocked out *Haus6* in proliferating apical progenitors in the embryonic mouse brain using nestin promotor-driven Cre expression. We found that augmin is essential for brain development, promoting mitotic progression and preventing p53-dependent apoptosis in neural progenitors. Intriguingly, while absence of p53 promoted growth in *Haus6* knockout brains, this was accompanied by exacerbated mitotic errors and

disruption of tissue integrity. Our results show that contrary to centrosomal microtubule nucleation, the augmin-dependent pathway is essential for apical progenitor mitotic progression and survival, and thus for brain development.

Results

Augmin is essential for proper development of the mouse forebrain

Previous work has shown that the augmin complex is composed of eight subunits and that depletion of any subunit interferes with augmin assembly and function (Goshima et al., 2008; Lawo et al., 2009; Uehara et al., 2009). Mouse embryos that completely lack expression of the augmin subunit *Haus6* do not survive the blastocyst stage (Watanabe et al., 2016). In order to test the specific requirement for augmin in proliferating neural progenitors, we obtained floxed *Haus6* mice in which exon 1 of the *Haus6* gene is flanked by loxP sequences (Watanabe et al., 2016). To generate *Haus6* conditional knockout (*Haus6* cKO) mice for the current study, we removed the neomycin cassette that was present in the original strain adjacent to exon 1 (see Materials and Methods for details). We then crossed these mice with mice expressing Cre recombinase under control of the Nestin promoter, to induce *Haus6* knockout in apical progenitors starting around day E10.5 (Figure 1a; Figure 1-figure supplement 1a) (Graus-Porta et al., 2001; Tronche et al., 1999). In contrast to the full knockout (Watanabe et al., 2016), *Haus6* cKO mice passed through all developmental stages and at E13.5 we observed efficient deletion of *Haus6* in the brain (Figure 1-figure supplement 1b). Whereas mice with a heterozygous *Haus6* deletion developed normally and were fertile*, homozygous Haus6 c*KO mice died around birth. Analysis of *Haus6* cKO animals at E17.5 showed severe defects in

147 brain development, whereas overall body development appeared normal (Figure 1b,
148 c; Figure 1-figure supplement 1c). Histopathology analysis revealed a strong
149 disruption or absence of different forebrain structures (cortex, thalamus,
150 hypothalamus) and of the cerebellum (Figure 1c; Figure 1-figure supplement 1c). To
151 evaluate whether this was due to agenesis or tissue loss during development, we
152 analyzed embryos at E13.5. Even at this earlier stage brains in *Haus6* cKO embryos
153 displayed severe defects compared to control embryos. Lateral cortexes in *Haus6*
154 cKO embryos were almost completely absent and thalamus structures, while partially
155 formed, displayed a strong reduction in radial thickness (Figure 1d, f). Moreover,
156 spaces between tissue structures were filled with cellular debris. These data suggest
157 that, in *Haus6* cKO brains at early developmental stages, formation of structures that
158 would give rise to the cortex, thalamus and hypothalamus is initiated but not
159 completed, leading to tissue loss and abortion of brain development at later stages.
160
161 **Loss of augmin impairs mitotic progression in cortical and thalamic neural**
162 **progenitors**
163 To analyze defective brain development in *Haus6* cKO animals at E13.5 at the
164 cellular level we focused on the thalamus, which was at least partially preserved. We
165 co-stained brain sections with antibodies against PAX6 and βIII-tubulin to label apical
166 progenitors and neurons, respectively. In *Haus6* cKO embryos we observed that the
167 reduced radial thickness in the thalamus was due to a striking thinning of the
168 neuronal layer by ~90% when compared to controls (Figure 1e, f), indicating severely
169 impaired neurogenesis. In some parts, where tissue organization appeared to be
170 disrupted, we also observed neurons that were misplaced in apical regions (Figure
171 1e). To directly test if augmin deficiency impaired mitoses, we identified and

quantified mitotic cells in the thalamus using Ser10-phospho-Histone H3 staining. In *Haus6* cKO embryos we observed a ~4-fold increase in the number of mitotic cells in the region closest to the ventricular surface compared to controls, whereas there were no significant differences in more basal regions (Figure 2a, b). The percentage of *Haus6* cKO mitotic cells in prometaphase was strongly increased, whereas metaphases and ana/telophases were reduced relative to controls (Figure 2c; Figure 2-figure supplement 1a). This increase in early and decrease in later mitotic figures was consistent with a delay in spindle assembly. Together these observations suggest that augmin deficiency in progenitors of the thalamus leads to a defect in progression to metaphase, causing mitotic delay.

To analyze cortical progenitors and since there were no intact cortical structures in *Haus6* cKO brains at E13.5, we analyzed embryos at E11.5. At this stage cortical structures were present suggesting that, as for the thalamus, cortical tissue is originally formed but lost at later stages. Similar to the situation in the thalamus at E13.5, in *Haus6* cKO cortexes at E11.5 the percentage of mitotic progenitors was increased when compared to controls and this occurred specifically in the apical region and not in more basal layers. Again, this increase in mitotic cells was due to accumulation in prometaphase (Figure 2-figure supplement 1b-e). Together the data show that augmin plays an important role in allowing timely mitotic progression of apical progenitors in different regions of the developing mouse brain.

To test if augmin-deficient progenitors displayed spindle defects we analyzed brain sections with antibodies against γ-tubulin and α-tubulin (Figure 2d-i). Mitotic apical progenitors in the thalamus of control animals displayed strong, centrosomal staining of γ-tubulin at spindle poles and more diffuse γ-tubulin signals along spindle microtubules. In *Haus6* cKO embryos γ-tubulin could not be detected on spindle

197 microtubules. Moreover, in ~50% of cells the staining of γ-tubulin at spindle poles
198 was dispersed into multiple smaller foci (Figure 2d, e). Some of these foci were not
199 associated with centrioles, as revealed by centrin staining, suggesting that they
200 resulted from PCM fragmentation rather than centrosome amplification (Figure 2-
201 figure supplement 1f). Consistent with this, centriole numbers in *Haus6* cKO cells
202 were not increased compared to controls (Figure 2-figure supplement 1g). Similar
203 observations were previously made by knockdown of augmin subunits in cell lines
204 (Lawo et al., 2009). Labeling of microtubules by α-tubulin antibodies revealed spindle
205 abnormalities in about half of the mitotic progenitors in *Haus6* cKO animals (Figure
206 2f, g). This included cases where spindle microtubules could not be detected (Figure
207 2h, i), suggesting decreased stability as previously reported (Goshima et al., 2008;
208 Lawo et al., 2009; Zhu et al., 2008). Defective spindles in *Haus6* cKO cells lacked the
209 bipolar configuration with two robust and focused microtubule asters typically seen in
210 controls. Instead, spindle microtubules were associated with multiple, scattered γ-
211 tubulin foci, resulting in spindles that appeared disorganized, sometimes with multiple
212 poles (Figure 2f). However, bipolar configurations including at ana/telophase were
213 also observed and cell divisions occurred in *Haus6* cKO progenitors, suggesting that
214 mitosis was not completely blocked.

215 Considering that augmin-deficiency caused pole fragmentation, we wondered
216 whether this affected spindle positioning. We measured spindle angles relative to the
217 ventricular surface in dividing apical progenitors in the thalamus and in the cortex of
218 E13.5 and E11.5 *Haus6* cKO embryos, respectively. We found that in both cases the
219 majority of spindles axes were oriented horizontally similar to spindles in control cells
220 (Figure 2-figure supplement 2h-j). This is consistent with results from previous work

showing that the presence of multiple spindle poles in progenitors due to extra centrosomes does not significantly affect spindle orientation (Marthiens et al., 2013).

In summary, augmin deficiency in apical progenitors disrupts recruitment of γ-tubulin to spindle microtubules, causes pole fragmentation, and interferes with bipolar spindle assembly and mitotic progression.

Loss of augmin in neural progenitors induces p53 expression and apoptosis

We sought to determine the fate of progenitors undergoing abnormal mitoses after loss of augmin. We probed thalamus and cortex of E13.5 and E11.5 *Haus6* cKO embryos, respectively, for p53 induction and the presence of the apoptotic marker cleaved caspase-3. Indeed, p53 and cleaved caspase-3 were strongly upregulated in both brain regions (Figure 2j, k; Figure 2-figure supplement 2a), whereas cells positive for these markers were barely found in the corresponding tissues of control embryos. To reveal the identity of cells overexpressing p53, we performed a triple staining with antibodies against p53, the neuronal marker βIII-tubulin and the apical progenitor marker PAX6 (Figure 2l). This experiment showed that in the *Haus6* cKO thalamus ~87% of the p53-positive cells were also positive for PAX6 and only a minor fraction (~5%) for βIII-tubulin (Figure 2m). Moreover, we observed that PAX6-positive progenitors displaying p53 induction were exclusively interphase cells, based on the presence of intact nuclei. We concluded that p53 induction occurred specifically in augmin-deficient progenitors, after exit from abnormal mitoses. Interestingly, some cells in the thalamus of *Haus6* cKO embryos also displayed upregulated expression of the cell cycle inhibitor p21 (Figure 2-figure supplement 2b,c).

Together the data suggests that mitotic spindle defects in *Haus6* cKO progenitors are not catastrophic *per se*, but efficiently trigger cell cycle arrest and apoptotic cell death upon completion of mitosis.

Co-deletion of *Trp53* in *Haus6* cKO embryos rescues apoptosis but not forebrain development

Since massive apoptosis in *Haus6* cKO brains was correlated with p53 induction, we wondered whether cell death was p53-dependent and the cause of aborted brain development. To address this, we crossed *Haus6* cKO mice with *Trp53* KO mice (Figure 3a). Strikingly, at E13.5, a stage at which *Haus6* cKO brains displayed massive apoptosis, lacked cortical structures and had a poorly developed thalamus, *Haus6* cKO *Trp53* KO brains showed only minimal signs of apoptosis and there was some growth in the regions where cortex and thalamus would be expected to form (Figure 3b-d). Consistent with this, there was also no upregulation of p21 (Figure 3-figure supplement 1a-d). Tissue growth was enhanced when compared to the single *Haus6* cKO brains, but seemed to lack the layered organization observed in control brains at this stage (Figure 3b). At E17.5, however, when thalamus and cortex were well formed in controls, in *Haus6* cKO *Trp53* KO embryos cortex and thalamus structures appeared thin and undeveloped (Figure 3e). Moreover, as observed for *Haus6* cKO embryos, *Haus6* cKO *Trp53* KO animals were not viable and died around birth.

In summary, massive apoptosis and cell cycle arrest in *Haus6* cKO brains are rescued in *Haus6* cKO *Trp53* KO brains, promoting growth in the affected brain regions, but this growth is not productive for proper brain development.

Loss of p53 exacerbates mitotic defects caused by augmin deficiency

Next, we examined how co-deletion of *Haus6* and *Trp53* affected mitosis in proliferating progenitors. Similar to *Haus6* cKO alone (Figure 2), *Haus6* cKO *Trp53* KO embryos also had an increased density of mitotic cells in the cortex and the thalamus as revealed by Ser10-phospho-Histone H3 staining (Figure 4a-c). The majority of these cells were in prometaphase (Figure 4d) and had disorganized spindles with fragmented spindle poles (Figure 4-figure supplement 1a-d). While these defects were overall similar to those observed in *Haus6* cKO brains, we also observed some differences. Centrin staining showed that ~30% of mitotic *Haus6* cKO *Trp53* KO cells had an increased number of centrioles, indicating the presence of extra centrosomes (Figure 4-figure supplement 1e, f). Mitotic cells with extra centrosomes had a ~twofold increased size compared to cells with normal centrosome number (Figure 4-figure supplement 1g), suggesting that these cells had previously failed cytokinesis, as observed in augmin-depleted cultured cells (Uehara et al., 2009). Consistent with abnormal cell divisions, we also observed various abnormalities in post-metaphase cells. Compared to *Trp53* KO control littermates there was a strong increase in the number of defective anaphases and telophases including multipolar spindle configurations, lagging chromosomes and micronuclei formation (Figure 4e-g). We also noticed that a fraction of *Haus6* cKO progenitors displayed enlarged nuclei in interphase (Figure 4h), suggesting aneuploidy/polyploidy triggered by abnormal chromosome segregation and/or failed cytokinesis. Considering that there were very few apoptotic cells in the double KO brains (Figure 3c), we speculated that continued proliferation may exacerbate mitotic defects. We analyzed multipolar metaphases and abnormal anaphase and telophases in *Haus6* cKO and *Haus6* cKO *Trp53* KO embryos at E13.5 in the thalamus, a structure that

was present in embryos of both genotypes at this stage. We found that mitotic defects were more severe in the *Haus6* cKO *Trp53* KO brains when compared to *Haus6* cKO brains (Figure 4i, j).

Mitotic errors in augmin-deficient progenitors correlate with DNA damage

Since mitotic errors can cause DNA breaks (Quignon et al., 2007), we probed brain tissue of *Haus6* cKO *Trp53* KO embryos for the presence of γH2AX foci, a marker of an active DNA damage response. Indeed, at E13.5 the percentage of cells with interphase nuclei displaying DNA damage was strongly increased in both the cortex and thalamus when compared to controls (Figure 5a-d). Side-by-side comparison of γH2AX staining in E13.5 thalamus of *Haus6* cKO and *Haus6* cKO *Trp53* KO embryos showed that augmin deficiency led to increased DNA damage relative to controls and that absence of p53 further increased this effect (Figure 5c, d). Thus, the extent of mitotic defects that we observed in *Haus6* cKO and *Haus6* cKO *Trp53* KO embryos was correlated with a concomitant increase in DNA damage.

Augmin deficiency reduces neurogenesis

Centrosome defects result in premature differentiation in human cerebral organoid models (Gabriel et al., 2016; Lancaster et al., 2013). We wondered whether premature differentiation may contribute to the defects observed in augmin-deficient mouse brains. To address this, we labeled embryonic apical progenitors in S phase by BrdU injection into pregnant mice at E12.5 and sacrificed the embryos for analysis 24 h later (Figure 6a). We then determined among the BrdU-positive cells the proportion that had exited the cell cycle (negative for Ki67 staining) or that underwent neuronal differentiation (negative for PAX6 staining, positive for βIII-tubulin staining)

in cortex and thalamus (Figure 6b-e). We observed that compared to controls the proportion of BrdU-positive, βIII-tubulin expressing cells was reduced in both *Haus6* cKO and *Haus6* cKO *Trp53* KO brains. This result suggested that mitotic defects caused by augmin deficiency did not result in premature differentiation but rather interfered with neurogenesis, and that this was not rescued by co-deletion of *Trp53*.

Loss of augmin in *Trp53* KO brains disrupts neuroepithelium integrity

Apart from the aberrant mitoses in *Haus6* cKO *Trp53* KO progenitors, the distribution of mitotic figures within the tissue was also highly abnormal. Whereas in control and *Haus6* cKO brains the vast majority of mitotic figures with condensed chromosomes were observed in the apical region, near the ventricular surface (Figure 2a, b; Figure 2-figure supplement 1b, d), in *Haus6* cKO *Trp53* KO brains most of the mitotic figures were distributed throughout the tissue including more basal regions (Figure 4a-c).

The presence of large numbers of basally positioned mitotic figures in the cortex and thalamus of *Haus6* cKO *Trp53* KO embryos could indicate that apical progenitors had delaminated, that their nuclei did not migrate to the apical region prior to division, or that the cells displaying mitotic defects in basal layers were not apical progenitors. The latter possibility was tested by PAX6 staining (Figure 7a). Whereas in the cortex of *Trp53* KO controls PAX6-positive cells were confined to the ventricular zone, well separated from more basally positioned neurons labelled by βIII-tubulin staining, in *Haus6* cKO *Trp53* KO cortex PAX6-positive cells localized indiscriminately in basal and apical regions of the cortex, largely overlapping with regions populated by βIII-tubulin-positive neurons (Figure 7a, d). Interestingly, TBR2-positive intermediate progenitors, residing in the subventricular zone in control sections, had also lost this confined localization in *Haus6* cKO *Trp53* KO cortexes

(Figure 7b, e). During development, apical progenitors in interphase maintain a bipolar structure with their centrosomes lining the ventricular surface, a configuration that is readily visualized by γ-tubulin staining in control embryos (Figure 7c). In *Haus6* cKO *Trp53* KO embryos apical centrosome localization was strongly reduced and sometimes completely lost (Figure 7c, f). Instead, clusters of γ-tubulin foci were observed in subventricular regions, where they were never observed in controls (Figure 7c). Centrin staining indicated the presence of many centrioles, confirming that these were clustered centrosomes rather than PCM fragments (figure 7-figure supplement 1a). Together these observations suggested that progenitors in *Haus6* cKO *Trp53* KO cortexes were not only incorrectly positioned, but had also lost their polar organization. To assess this more directly, we stained for nestin, an intermediate filament protein specifically expressed in apical progenitors. In the cortex of control embryos, nestin-stained progenitors displayed a highly polarized, apico-basal morphology and a laterally aligned arrangement within the tissue (Figure 7-figure supplement 2a). In contrast, polarized morphology and lateral alignment were completely disrupted in progenitors of *Haus6* cKO *Trp53* KO embryos (Figure 7-figure supplement 2a). Consistent with these observations, staining with α-tubulin antibodies revealed that microtubules displayed apico-basal organization in control cells, running along the length of the highly polarized cell bodies (Figure 7-figure supplement 2b, c). In contrast, microtubules in *Haus6* cKO *Trp53* KO progenitors lacked apico-basal orientation and appeared disorganized (Figure 7-figure supplement 2b, c).

Together these data suggest that in *Haus6* cKO *Trp53* KO embryos apical progenitors had lost their polarized organization and divided ectopically. As a result, neuroepithelium integrity was severely disrupted.

Discussion

The mitotic spindle serves to segregate the replicated chromosomes faithfully into two daughter cells. This task is carried out by spindle microtubules and a multitude of proteins that nucleate, organize and remodel these microtubules during mitotic progression. Here we have analyzed the contribution of one of three different microtubule nucleation pathways, augmin-mediated microtubule amplification, to mitotic spindle assembly in proliferating neural progenitor cells during mouse brain development. Previous work found that impairment of centrosomal microtubule nucleation in apical progenitors slowed mitotic spindle assembly and progression, leading to p53-dependent apoptosis and causing microcephaly (Insolera et al., 2014; Lin et al., 2020; Marjanović et al., 2015; McIntyre et al., 2012; Novorol et al., 2013). Similarly, we found that augmin-deficiency also impaired spindle assembly, delayed mitosis, and induced p53-dependent apoptosis. In agreement with previous functional studies in cell lines (Lawo et al., 2009), augmin-deficient progenitors displayed fragmented spindle poles, but this did not significantly impair spindle positioning. The most important outcome of these defects was cell death. Our finding that the large majority of cells positive for expression of p53 and the apoptotic marker cleaved caspase-3 were PAX6-positive interphase cells, suggests that cell death occurred after completion of abnormal mitoses. Despite the similarities with centrosome defects, the *Haus6* conditional knockout phenotype is much more severe. Rather than leading to microcephaly, augmin deficiency completely aborted brain development. To our knowledge this has not been reported for any other microtubule regulator affecting mitotic spindle assembly and progression. How can

this be explained? While mitotic defects and apoptosis were also observed after loss of centrioles by conditional *CenpJ/Cpap/Sas4* knockout (Insolera et al., 2014) and amplification of centrosome number by PLK4 overexpression (Marthiens et al., 2013), the specific spindle defects caused by augmin deficiency may be a more potent trigger of apoptotic cell death than defects resulting from centrosome abnormalities. It should be noted that a more recent *Cenpj* conditional knockout mouse model displayed more severe disruption of forebrain structures, causing lethality a few weeks after birth (Lin et al., 2020). Still, these defects seem less severe than what we observed after augmin knockout. One may expect that preventing cell death in augmin-deficient progenitors would, at least to some degree, rescue brain development. Codeletion of *Trp53* in *Haus6* cKO mice largely rescued apoptosis, revealing that cell death was p53-dependent, but did not rescue brain development and lethality. In the absence of apoptosis, augmin-deficient progenitors likely underwent repeated cycles of abnormal mitoses, leading to increasingly severe mitotic abnormalities. This behavior has recently been described after induced knockout of the augmin subunit *HAUS8* in the RPE1 cell line. Whereas *HAUS8* knockout in a *TRP53* wild type background only mildly impaired mitosis before cells arrested in G1, co-deletion of *TRP53* eliminated cell cycle arrest and exacerbated mitotic defects (McKinley and Cheeseman, 2017). Consistent with this possibility, *Haus6* cKO *Trp53* KO progenitors had more severe mitotic defects than *Haus6* cKO cells, including lagging chromosomes and multipolar spindles at post-metaphase stages, and displayed increased DNA damage. We have not formally tested whether cell death in augmin-deficient progenitors involves the recently described, USP28-53BP1-p53-p21-dependent mitotic surveillance pathway (Lambrus and Holland, 2017). However, our results show that during brain development cells that have

undergone erroneous mitosis are efficiently eliminated in a p53-dependent manner, and that this occurs independently of whether the cause is centrosomal or non-centrosomal. The situation may be different in human brain development, where premature differentiation rather than apoptosis was shown to be the main response to centrosome defects in microcephaly organoid models (Gabriel et al., 2016; Lancaster et al., 2013). How human brain development would be affected by augmin deficiency is unclear. However, considering the severity of the *Haus6* KO phenotype in mice, augmin deficiency may also be lethal in humans.

The pole-fragmentation phenotype in augmin-deficient mitotic progenitors may be comparable to mitoses in the presence of extra centrosomes, as described in mice overexpressing PLK4 (Marthiens et al., 2013). In these animals co-deletion of *Trp53* also exacerbated mitotic defects and aneuploidy, but the outcome was still a microcephalic brain (Marthiens et al., 2013). In contrast, in the case of *Haus6* cKO *Trp53* KO progenitors in our study, continued proliferation was not productive for brain development. While some cortical structures were present at E13.5, they lacked a pseudostratified epithelial organization. Progenitors had lost their characteristic, highly polarized morphology and formed a disorganized cell mass that was intermingled with βIII-tubulin-positive differentiated neurons, in both apical and basal regions. Considering that the polarized apical progenitor morphology is integral to the organization of the neuroepithelium, providing scaffold function and guidance for translocating basal progenitors and migrating neurons, it is not surprising that these defects lead to abortion of brain development.

Exacerbated mitotic errors and DNA damage as a result of continued proliferation are a reasonable explanation for the severely disrupted tissue integrity in *Haus6* cKO *Trp53* KO brains. However, we cannot exclude that additional roles of

augmin contribute to this phenotype. For example, augmin may promote progenitor polarity by generating and/or maintaining the apico-basal interphase microtubule array. Recent work has shown that experimentally altered spindle positioning in progenitors can lead to loss of apical membrane. This can be compensated for by re-extension of the apical process and re-integration of the apical foot at the ventricular surface (Fujita et al., 2019). Assuming a role of augmin in progenitor polarity, this process may be impaired in augmin-deficient cells. Consistent with this possibility, microtubules in *Haus6* cKO *Trp53* KO progenitors appeared disorganized, lacking the apico-basal alignment that is observed in control cells. However, it is unclear whether this is cause or consequence of the loss of polarized cell morphology. It should also be noted that augmin nucleates microtubules in post-mitotic neurons, affecting their morphogenesis and their migration (Cunha-Ferreira et al., 2018; Sánchez-Huertas et al., 2016), which could contribute to tissue disruption in *Haus6* cKO *Trp53* KO brains.

In summary, our work shows that, in contrast to centrosomal nucleation, augmin-mediated microtubule amplification in neural apical progenitors is essential for brain development and cannot be compensated for by the chromatin- and centrosome-dependent nucleation pathways. As in the case of progenitors lacking centrosomal nucleation, mitotic delay caused by augmin deficiency triggers p53-dependent apoptosis. While cell death can be prevented by co-deletion of *Trp53*, the specific defects that result from the loss of augmin are sufficient to completely abort brain development, independent of p53 status.

Materials and Methods

Key Resources Table				
Reagent type (species) or resource	**Designation**	**Source or reference**	**Identifiers**	**Additional information**
gene (*Mus musculus*)	*Haus6*	NCBI Gene	Gene ID: 230376	
strain, strain background (*Mus musculus*)	Nestin-Cre *Haus6* cKO	this paper		see method section
strain, strain background (*Mus musculus*)	Nestin-Cre *Haus6* cKO *Trp53* KO	this paper		see method section
strain, strain background (*Mus musculus*)	*Haus6* floxed Neo (*Haus6*$^{fl\text{-}Neo}$)	RIKEN http://www2.clst.riken.jp/arg/mutant%20mice%20list.html	CDB1218K	
strain, strain background (*Mus musculus*)	*Haus6* floxed *(Haus6*^{fl}*)*	RIKEN http://www2.clst.riken.jp/arg/mutant%20mice%20list.html	CDB1354K RRID:IMSR_RBRC09630	
strain, strain background (*Mus musculus*)	C57BL/6-Tg(CAG-flpe)36Ito/ItoRbrc	RIKEN (Kanki et al., 2006)	RRID:IMSR_RBRC01834	
strain, strain background (*Mus musculus*)	B6.Cg-Tg(Nes-cre)1Kln/J	Gift from Maria Pia Cosma (originally from Jackson Laboratories)	RRID:IMSR_JAX:003771	
strain, strain background (*Mus musculus*)	*Trp53*-deficient mice (B6.129S2-Trp53tm1Tyj/J)	Jackson Laboratories	RRID:IMSR_JAX:002101	
antibody	Anti-α-tubulin (mouse monoclonal)	Sigma	#3873T	IF (1:500)
antibody	Anti-acetylated α-tubulin (mouse monoclonal)	Sigma	#T6793 RRID:AB_477585	IF (1:500)
antibody	Anti-βIII-tubulin (rabbit	Abcam	#ab18207 RRID:AB_444319	IF (1:1000)

	polyclonal)			
antibody	Anti-βIII-tubulin (mouse monoclonal)	Biolegend	#801201 RRID:AB_2313773	IF (1:1000)
antibody	Anti-cleaved caspase-3 (rabbit monoclonal)	Novus Biologicals	#MAB835 RRID:AB_2243951	IF (1:500)
antibody	Anti-BrdU (mouse monoclonal)	Abcam	#ab8955 RRID:AB_306886	IF (1:750)
antibody	Anti-γ-tubulin (mouse monoclonal, clone TU-30)	ExBio	#ab27074 RRID:AB_2211240	IF (1:500)
antibody	Anti-γ-tubulin (rabbit monoclonal)	Sigma	#T5192 RRID:AB_261690	IF (1:500)
antibody	Anti-Ki67 (rabbit polyclonal)	Abcam	#ab15580 RRID:AB_443209	IF (1:750)
antibody	Anti-nestin (mouse monoclonal)	Cell signaling	#4760 RRID:AB_2235913	IF (1:300)
antibody	Anti-p53 (mouse monoclonal)	Cell signaling	#CST2524S RRID:AB_331743	IF (1:500)
antibody	Anti-PAX6 (mouse monoclonal)	Biolegend	#901301 RRID:AB_2565003	IF (1:300)
antibody	Anti-phosphorylated-Histone H3 (rabbit polyclonal)	Millipore	#06-570 RRID:AB_310177	IF (1:1000)
antibody	Anti-TBR2 (rabbit polyclonal)	Abcam	#ab23345 RRID:AB_778267	IF (1:200)
antibody	Anti-phospho-histone H2AX (Ser139) (mouse monoclonal, clone JBW301)	Millipore	#05-636 RRID:AB_309864	IHC (1:500)
antibody	Anti-p21 (rat monoclonal, HUGO291)	Abcam	#ab107099 RRID:AB_10891759	IHC (1:500)

antibody	Anti-centrin-Alexa 488 (rabbit polyclonal)	homemade (Andrew Holland) (Phan et al., 2021)		IF (1:500)
antibody	Anti-mouse IgG Alexa 488 (goat polyclonal)	Life Technologies	#A11029 RRID:AB_138404	IF (1:500)
antibody	Anti-mouse IgG1 Alexa 488 (goat polyclonal)	Life Technologies	#A21121 RRID:AB_2535764	IF (1:500)
antibody	Anti-mouse IgG1 Alexa 568 (goat polyclonal)	Life Technologies	#A21124 RRID:AB_2535766	IF (1:500)
antibody	Anti-mouse IgG1 Alexa 633 (goat polyclonal)	Life Technologies	#A21052 RRID:AB_2535719	IF (1:500)
antibody	Anti-mouse IgG2a Alexa 488 (goat polyclonal)	Life Technologies	#A21131 RRID:AB_2535771	IF (1:500)
antibody	Anti-rabbit IgG Alexa 488 (goat polyclonal)	Life Technologies	#A11034 RRID:AB_2576217	IF (1:500)
antibody	Anti-rabbit IgG Alexa 568 (goat polyclonal)	Life Technologies	#A11036 RRID:AB_10563566	IF (1:500)
antibody	Anti-rabbit IgG Alexa 633 (goat polyclonal)	Life Technologies	#A21071 RRID:AB_141419	IF (1:500)
antibody	Anti-mouse IgG HRP conjugated (goat polyclonal)	Dako-Agilent	#P0447 RRID:AB_2617137	IHC (1:500)
antibody	Rabbit IgG polyclonal isotype control (rabbit polyclonal)	Abcam	#ab27478 RRID:AB_2616600	IHC (1:500)
antibody	Mouse IgG1 (NCG01) isotype control (mouse monoclonal)	Abcam	#ab81032 RRID:AB_2750592	IHC (1:500)
antibody	Mouse IgG2a	Invitrogen	#14-4724-82	IHC (1:500)

	isotype control (eBM2a) (mouse monoclonal)		RRID:AB_470114	
sequence-based reagent	mAug6KO_FW	this paper	genomic PCR primer *Haus6*	5'-CAACCCGAGCAACAGAAACC-3'
sequenced-based reagent	mAug6KO_Rev	this paper	genomic PCR primer *Haus6*	5'-CCTCCCACCAACTACAGACC-3'
sequenced-based reagent	olMR1084	this paper	genomic PCR primer *Cre*	5'-GCGGTCTGGCAGTAAAAACTATC-3'
sequenced-based reagent	olMR1085	this paper	Genomic PCR primer *Cre*	5'-GTGAAACAGCATTGCTGTCACTT-3'
sequenced-based reagent	olMR7338	this paper	Genomic PCR primer control	5'-CTAGGCCACAGAATTGAAAGATCT-3'
sequenced-based reagent	olMR7339	this paper	Genomic PCR primer control	5'GTAGGTGGAAATTCTAGCATCATCC-3'
software, algorithm	GraphPad Prism	GraphPad Software Inc.	RRID:SCR_002798	
software, algorithm	QuPath	Queens University (Belfast,UK)	RRID:SCR_018257	
software, algorithm	FIJI (ImageJ)	NIH	RRID:SCR_002285	
other	hematoxylin	Dako-Agilent	S202084	
other	5-Bromo-2'-deoxyuridine (BrdU)	Sigma	B5002	injected peritoneally to pregnant females at a final concentration of 120 mg/kg of animal weight
other	EnVision Flex Antibody Diluent	Dako-Agilent	K800621	
other	Envision Flex	Dako-Agilent	K800721	

	Wash buffer			
other	3-3′-diamino-benzidine	Dako-Agilent	K3468	
commercial assay or kit	Mouse on mouse (M.O.M) Immuno-detection Kit	Vector Laboratories	BMK-2202 RRID:AB_2336833	

Generation and husbandry of mice

Nestin-Cre *Haus6* cKO were obtained by crossing *Haus6* floxed (*Haus6*^{fl}) mice with B6.Cg-Tg(Nes-cre)1Kln/J mice. *Haus6* floxed Neo mice (*Haus6*$^{fl\text{-}Neo}$) (Acc. No. CDB1218K, http://www2.clst.riken.jp/arg/mutant%20mice%20list.html) were generated as described (Watanabe et al., 2016). To generate *Haus6* floxed mice (*Haus6*^{fl}) (RBRC09630, Accession No.CDB1354K (http://www2.clst.riken.jp/arg/mutant%20mice%20list.html), *Haus6*$^{fl\text{-}Neo}$ mice were crossed with C57BL/6-Tg(CAG-flpe)36Ito/ItoRbrc (RBRC01834) (Kanki et al., 2006). The resultant mice without the PGK-neo cassette (*Haus6* flox mice) were maintained by heterozygous crossing (C57BL/6N background). B6-Tg(CAG-FLPe)36 was provided by the RIKEN BRC through the National Bio-Resource Project of the MEXT, Japan. B6.Cg-Tg(Nes-cre)1Kln/J) mice were a gift from Maria Pia Cosma (CRG, Barcelona, Spain) and previously purchased from Jackson Laboratories. To obtain Nestin-Cre *Haus6* cKO *Trp53* KO mice, mice carrying the floxed *Haus6* (*Haus6*^{fl}) and Nestin-Cre alleles were crossed with mice lacking *p53*. *p53*-deficient mice (B6.129S2-Trp53tm1Tyj/J) were purchased from Jackson Laboratories. All the mouse strains were maintained on a mixed 129/SvEv-C57BL/6 background in strict accordance with the European Community (2010/63/UE) guidelines in the Specific-Pathogen Free (SPF) animal facilities of the Barcelona Science Park (PCB). All protocols were approved by the Animal Care and Use Committee of the

PCB/University of Barcelona (IACUC; CEEA-PCB) and by the Departament de Territori I Sostenibilitat of the Generalitat de Catalunya in accordance with applicable legislation (Real Decreto 53/2013). All efforts were made to minimize use and suffering.

Mice Genotyping

Genotyping was performed by PCR using genomic DNA extracted from tail or ear biopsies. Biopsies were digested with Proteinase-K (0.4 mg/mL in 10 mM Tris-HCl, 20 mM NaCl, 0.2% SDS, 0.5 mM EDTA) overnight at 56°C. DNA was recovered by isopropanol precipitation, washed in 70% ethanol, dried and resuspended in H_2O. To detect *Haus6* wt (800 bp), *Haus6* floxed (1080 bp) and *Haus6* KO (530 bp) alleles by PCR the following pair of primers was used: mAug6KO_FW (5'-CAACCCGAGCAACAGAAACC-3') and mAug6KO_Rev (5'-CCTCCCACCAACTACAGACC-3'). These PCRs were run for 35 cycles with an annealing temperature of 64.5°C. To detect the transgenic Cre-recombinase allele in Nestin-Cre cKO mice (100bp) primers olMR1084 (5'-GCGGTCTGGCAGTAAAAACTATC-3') and olMR1085 (5'-GTGAAACAGCATTGCTGTCACTT-3') were used. For this PCR, primers olMR7338 (5'- CTAGGCCACAGAATTGAAAGATCT-3') and olMR7339 (5'-GTAGGTGGAAATTCTAGCATCATCC-3') were used as internal control (324 bp). These PCRs were run for 35 cycles with an annealing temperature of 51.7°C.

BrdU injections

Pregnant females with embryos at E12.5 were injected intraperitoneally with 5-Bromo-2'-deoxyuridine (BrdU) (B5002; Sigma) diluted in PBS at a final concentration

of 120 mg per kg of animal weight. 24 hours later embryonic brain tissue was processed for histopathology analysis as described in the next section.

Histology, immunofluorescence and immunohistochemistry

For histopathology analysis of mouse embryos, timed pregnant female mice were euthanized and embryos were removed. Following euthanasia, embryo heads were fixed in 4% PFA diluted in PBS overnight at 4ºC, followed by cryoprotection in increasing concentration of sucrose in PBS (first 15%, then 30%, with a 24h incubation at 4ºC for each sucrose concentration), followed by an overnight incubation in a 1:1 solution of 30% sucrose and OCT (Tissue-Tek). Tissues were then embedded in OCT and frozen in liquid nitrogen-cooled isopentane. For tissue histological analysis, 10 µm thick cryosections were prepared, placed on glass slides and processed for either hematoxilin/eosin staining using standard protocols or for immunofluorescence staining. For immunofluorescence staining, cryosections were thawed at room temperature, washed with PBS and subjected to heat-mediated antigen retrieval in citrate buffer (10 mM citric acid) at pH6, as required. Tissue sections were permeabilized with PBS containing 0.05% TX100 (PBS-T 0.05%) for 15 minutes and blocked with blocking solution (10% goat serum diluted in PBS-T 0.1%). Sections were then incubated overnight at 4ºC with primary antibodies diluted in blocking solution. The next day, after washing with PBS-T 0.05%, sections were incubated for 60 minutes with Alexa-Fluor conjugated complementary secondary antibodies and DAPI to stain DNA. Sections were again washed with PBS-T 0.05% and mounted with Prolong Gold antifading reagent (Thermo Fisher).

For immunofluorescence stainings after BrdU incorporation sections were dried and fixed with neutral buffer formalin (HT501128-4L, Sigma-Aldrich) for 10 min. Antigen

retrieval was performed using citrate buffer pH 6 for 20 min at 97ºC using a PT Link (Dako – Agilent). Quenching of endogenous peroxidase was performed by incubation for 10 min with Peroxidase-Blocking Solution (S2023, Dako-Agilent). Unspecific unions were blocked using 5% of goat normal serum (16210064, Life technology) with 2.5% BSA (10735078001, Sigma) for 60min. Blocking of unspecific endogenous mouse Ig staining was also performed using Mouse on mouse (M.O.M) Immunodetection Kit – (BMK-2202, Vector Laboratories). Primary antibodies were diluted in EnVision FLEX Antibody Diluent (K800621, Dako-Agilent) and incubated overnight at 4ºC. Secondary antibodies were diluted at 1:500 and incubated for 60 min. Samples were stained with DAPI (D9542, Sigma) and mounted with Fluorescence mounting medium (S3023 Dako). Specificity of staining was confirmed by staining with rabbit IgG, polyclonal Isotype control (ab27478, Abcam), mouse IgG1, Kappa Monoclonal (NCG01) Isotype Control (ab81032, Abcam) or a mouse IgG2a kappa Isotype Control (eBM2a) (14-4724-82 IgM, Invitrogen).

Immunohistochemistry was performed using 7 µm cuts. Prior to immunohistochemistry antigen retrieval was performed using Tris-EDTA buffer pH 9 for 20 min at 97ºC using a PT Link (Dako – Agilent). Quenching of endogenous peroxidase was performed by a 10 min incubation with Peroxidase-Blocking Solution (Dako REAL S2023). Blocking was done in M.O.M. blocking reagent (MKB-2213, Vectorlabs), 5 % of goat normal serum (16210064, Thermo Fisher) mixed with 2.5 % BSA diluted in Envision Flex Wash buffer (K800721, Dako - Agilent) and with Casein solution (ref: 760-219, Roche) for 60 and 30 min, respectively. Primary and secondary antibodies were diluted with EnVision FLEX Antibody Diluent (K800621, Dako, Agilent) and incubated for 120 min. Antigen–antibody complexes were revealed with 3-3′-diaminobenzidine (K3468, Dako). Sections were counterstained

568 with hematoxylin (Dako, S202084) and mounted with Mounting Medium, Toluene-
569 Free (CS705, Dako) using a Dako CoverStainer. Specificity of staining was
570 confirmed by using a mouse IgG1 isotype control (ab81032, Abcam).
571
572 **Antibodies**
573 All antibodies are listed in the key resources table.
574
575 **Image acquisition and analysis**
576 Histology sections stained with hematoxilin/eosin (Figure 1c, d; Figure 1-figure
577 supplement 1c; Figure 3b, e) or used for immunohistochemistry (Figure 5a, c; Figure
578 2-figure supplement 2b; Figure 3-figure supplement 1a, c) were imaged with the
579 digital slide scanner Nanozoomer 2.0 HT from Hamamatsu and processed with
580 NDP.view 2 software from Hamamatsu. Immunofluorescence labeled histology
581 sections (Figure 1e; Figure 2a, d, h, j, l; Figure 2-figure supplement 1a, b, c, f, h;
582 Figure 2-figure supplement 2a; Figure 3c; Figure 4a, b; Figure 4-figure supplement
583 1a, c, e; Figure 6; Figure 7; Figure 7-figure supplement 1; Figure 7-figure supplement
584 2) were imaged with a Leica TCS SP5 laser scanning spectral confocal microscope.
585 Confocal Z-stacks were acquired with 0.5 µm or 1 µm of step size depending on the
586 experiment and using laser parameters that avoided the presence of saturated
587 pixels. Immunofluorescence-labeled histology sections shown in Fig. 2f and Fig. 4e
588 were imaged with a Zeiss 880 confocal microscope equipped with an Airyscan. In the
589 images shown in Fig. 2f, for the Superresolution Airyscan mode a 63x magnification,
590 1.4NA oil-immersion lens with a digital zoom of 1.8x was used. The z-step between
591 the stacks was set at 0.211 µm. In the images shown in Fig. 4e, for the Fast Airyscan
592 mode a 40x magnification 1.2 NA multi-immersion lens with a digital zoom of 1.8x

was used. The Z-step between the stacks was set at 0.5 µm. XY resolution was set at 1588x1588. Airyscan raw data were preprocessed with the automatic setting of Zen Black. Additional image processing and maximum intensity z-projections were done in ImageJ software. In each experiment, serial brain sections from multiple animals per genotype were analyzed (details in figure legends).

Radial thickness of the thalamus was measured with ImageJ as the distance between the ventricular surface and the basal surface of this brain region in E13.5 embryos. In the same regions, radial thickness of the area occupied by PAX6 and βIII-tubulin cell populations was measured.

For mitotic density cell counts the thalamic/cortical wall was divided into 30-µm thick bins from the apical to basal surfaces. The number of mitotic phospho-Histone H3 positive cells was counted in each bin and normalized to the column width of the region analyzed. Mitotic density in each bin was expressed as the number of mitotic cells per 100 µm of column. Centrosome integrity in mitotic cells dividing close to the apical surface of the thalamus/cortex was analyzed by quantifying the percentage of cells displaying unfocused/fragmented spindle poles, each composed of multiple γ-tubulin dots. Mitotic spindle integrity was analyzed in cells dividing close to the apical surface of the thalamus and the percentage of cells displaying abnormal, non-bipolar organized spindles was quantified.

To evaluate p53 expression, cell death, DNA-damage, cell cycle exit and neurogenesis in the embryonic forebrain, representative images of the thalamus/cortex containing the entire apico-basal axis of the tissue were selected. The number of p53 and cleaved caspase-3 positive cells was counted and divided by the area of the selected region. To evaluate the cell population overexpressing p53 in the thalamus, coronal sections were co-stained against p53, PAX6 and βIII-tubulin.

618 Cells in which the p53-positive nucleus was costained with PAX6 were counted as
619 PAX6-positive. Cells with p53-positive nucleus that did not stain for PAX6 and were
620 surrounded by a cytoplasmic βIII-tubulin signal were considered as βIII-tubulin-
621 positive. To evaluate the expression of phosphorylated Histone H2AX, image files
622 obtained with the Nanozoomer 2.0 HT slide scanner were opened with the image
623 analysis software QuPath (Bankhead et al., 2017). The number of phosphorylated
624 Histone H2AX-positive cells was divided by the total amount of hematoxylin-stained
625 cells in the specific tissue, counted using the QuPath software. To evaluate cell cycle
626 exit and neurogenesis, embryonic tissue sections obtained from pregnant females
627 injected with BrdU were co-stained with BrdU and Ki67 antibodies (for cell cycle exit
628 analysis) or BrdU, PAX6 and βIII-tubulin antibodies (for neurogenesis analysis). To
629 evaluate co-expression of the different markers, image files obtained with the
630 Nanozoomer 2.0 HT slide scanner were opened with the image analysis software
631 QuPath and the “Positive Cell Detection tool was used”. Cell cycle exit was analyzed
632 by determining the number of BrdU-positive cells that did not stain for the cell cycle
633 marker Ki67 relative to the total number of BrdU-positive cells in the respective
634 tissue. Neurogenesis was evaluated by determining the number of BrdU-positive
635 cells that were also positive for βIII-tubulin staining but negative for PAX6 staining
636 relative to the total number of BrdU-positive cells in the respective tissue. In all
637 experiments, for each brain at least two coronal tissue sections were quantified.
638 To measure interphase nucleus size in cortical neural progenitors (Fig. 4h),
639 tissue sections were immunostained with PAX6 antibodies and DAPI to label DNA.
640 The area of nuclei in PAX6-positive cells in the cortex was measured in z-stack
641 images using the “Positive cell detection” tool of QuPath software. Mitotic cells were
642 excluded from this analysis.

643 To quantify the distribution of neural progenitors within the cortex,
644 cryosections providing lateral views of the cortex were immunostained against PAX6
645 or TBR2. In both cases, the “Plot Analysis” tool of ImageJ was used to measure
646 signal intensity along the apico-basal axis of the cortex. Measurements were
647 grouped into 9.8 µm-wide bins and the average value for each bin was plotted as
648 percentage of the sum of all bin intensities.

649 For analysis of mitotic spindle orientation, cryosections providing coronal
650 views of the thalamus/cortex were immunostained with DAPI and the mitotic DNA
651 marker phosphorylated-Histone H3 and the centrosome/spindle pole marker γ-
652 tubulin. The orientation of the mitotic spindle was then determined by measuring the
653 angle between the pole-to-pole axis and the ventricular lining.

654

655 **Statistics**

656 All graphs with error bars are presented as means with standard deviation. To
657 determine statistical significance between samples, unpaired two-way Student t-test
658 was used. Statistical calculations and generation of graphs were performed in Excel
659 or Graphpad Prism6 (ns = not significant, * $P<0.05$, ** $P<0.01$, *** $P<0.001$).

660

661

662 **Acknowledgements**

663 We are grateful to Gohta Goshima (Nagoya University, Japan) for generously
664 providing floxed *Haus6* mice that were generated in his laboratory and for feedback
665 on the manuscript. We acknowledge excellent support by the IRB Barcelona
666 Histopathology and Advanced Digital Microscopy core facilities for help with sample
667 preparation and analysis, and by the Mouse Mutant Core facility for deriving floxed

Haus6 mice from sperm samples. We thank Travis Stracker (NIH-NCI, Bethesda, USA) for mouse cage space and discussion, Eduardo Soriano and Antoni Parcerisas (University of Barcelona, Spain) for technical help and discussions, Andrew Holland (Johns Hopkins University, Baltimore, USA) for anti-centrin antibodies, Pia Cosma (CRG, Barcelona, Spain) for providing Nestin-Cre mice, and Irina Matos (The Rockefeller University, New York, USA) for helpful comments on the manuscript.

References

Aguirre-Portolés C, Bird AW, Hyman A, Cañamero M, Pérez de Castro I, Malumbres M. 2012. Tpx2 controls spindle integrity, genome stability, and tumor development. *Cancer research* **72**:1518–1528. doi:10.1158/0008-5472.CAN-11-1971

Alfaro-Aco R, Thawani A, Petry S. 2020. Biochemical reconstitution of branching microtubule nucleation. *eLife* **9**. doi:10.7554/eLife.49797

Arai Y, Taverna E. 2017. Neural Progenitor Cell Polarity and Cortical Development. *Frontiers in cellular neuroscience* **11**:384. doi:10.3389/fncel.2017.00384

Bankhead P, Loughrey MB, Fernández JA, Dombrowski Y, McArt DG, Dunne PD, McQuaid S, Gray RT, Murray LJ, Coleman HG, James JA, Salto-Tellez M, Hamilton PW. 2017. QuPath: Open source software for digital pathology image analysis. *Scientific reports* **7**:16878. doi:10.1038/s41598-017-17204-5

Chenn A, Zhang YA, Chang BT, McConnell SK. 1998. Intrinsic polarity of mammalian neuroepithelial cells. *Mol Cell Neurosci* **11**:183–193. doi:10.1006/mcne.1998.0680

Chou F-S, Li R, Wang P-S. 2018. Molecular components and polarity of radial glial cells during cerebral cortex development. *CMLS Cellular and Molecular Life Sciences* **75**:1027–1041. doi:10.1007/s00018-017-2680-0

Cunha-Ferreira I, Chazeau A, Buijs RR, Stucchi R, Will L, Pan X, Adolfs Y, van der Meer C, Wolthuis JC, Kahn OI, Schätzle P, Altelaar M, Pasterkamp RJ, Kapitein LC, Hoogenraad CC. 2018. The HAUS Complex Is a Key Regulator

of Non-centrosomal Microtubule Organization during Neuronal Development. *Cell Reports* **24**:791–800. doi:10.1016/j.celrep.2018.06.093

Du L, Xu J, Li X, Ma N, Liu Y, Peng J, Osato M, Zhang W, Wen Z. 2011. Rumba and Haus3 are essential factors for the maintenance of hematopoietic stem/progenitor cells during zebrafish hematopoiesis. *Development (Cambridge, England)* **138**:619–629. doi:10.1242/dev.054536

Edzuka T, Yamada L, Kanamaru K, Sawada H. 2014. Identification of the Augmin Complex in the Filamentous Fungus Aspergillus nidulans. *PloS one*. doi:10.1371/journal.pone.0101471.s003

Fong CS, Mazo G, Das T, Goodman J, Kim M, O'Rourke BP, Izquierdo D, Tsou M-FB. 2016. 53BP1 and USP28 mediate p53-dependent cell cycle arrest in response to centrosome loss and prolonged mitosis. *eLife* **5**:E1491. doi:10.7554/eLife.16270

Fujita I, Shitamukai A, Kusumoto F, Mase S, Suetsugu T, Omori A, Kato K, Abe T, Shioi G, Konno D, Matsuzaki F. 2019. Endfoot regeneration restricts radial glial state and prevents translocation into the outer subventricular zone in early mammalian brain development. *Nature cell biology* **22**:26–37. doi:10.1038/s41556-019-0436-9

Gabriel E, Wason A, Ramani A, Gooi LM, Keller P, Pozniakovsky A, Poser I, Noack F, Telugu NS, Calegari F, Šarić T, Hescheler J, Hyman AA, Gottardo M, Callaini G, Alkuraya FS, Gopalakrishnan J. 2016. CPAP promotes timely cilium disassembly to maintain neural progenitor pool. *The EMBO Journal* **35**:803–819. doi:10.15252/embj.201593679

Goshima G, Kimura A. 2010. New look inside the spindle: microtubule-dependent microtubule generation within the spindle. *Curr Opin Cell Biol* **22**:44–49. doi:10.1016/j.ceb.2009.11.012

Goshima G, Mayer M, Zhang N, Stuurman N, Vale RD. 2008. Augmin: a protein complex required for centrosome-independent microtubule generation within the spindle. *The Journal of cell biology* **181**:421–429. doi:10.1083/jcb.200711053

Graus-Porta D, Blaess S, Senften M, Littlewood-Evans A, Damsky C, Huang Z, Orban P, Klein R, Schittny JC, Müller U. 2001. Beta1-class integrins regulate the development of laminae and folia in the cerebral and cerebellar cortex. *Neuron* **31**:367–379. doi:10.1016/s0896-6273(01)00374-9

Gueth-Hallonet C, Antony C, Aghion J, Santa-Maria A, Lajoie-Mazenc I, Wright M, Maro B. 1993. gamma-Tubulin is present in acentriolar MTOCs during early mouse development. *J Cell Sci* **105 (Pt 1)**:157–166.

Hayward D, Metz J, Pellacani C, Wakefield JG. 2014. Synergy between multiple microtubule-generating pathways confers robustness to centrosome-driven mitotic spindle formation. *Developmental Cell* **28**:81–93. doi:10.1016/j.devcel.2013.12.001

Homem CCF, Repic M, Knoblich JA. 2015. Proliferation control in neural stem and progenitor cells. *Nature Reviews Neuroscience* **16**:647–659. doi:10.1038/nrn4021

Insolera R, Bazzi H, Shao W, Anderson KV, Shi S-H. 2014. Cortical neurogenesis in the absence of centrioles. *Nature neuroscience* **17**:1528–1535. doi:10.1038/nn.3831

Jayaraman D, Bae B-I, Walsh CA. 2018. The Genetics of Primary Microcephaly. *Annual review of genomics and human genetics* **19**:177–200. doi:10.1146/annurev-genom-083117-021441

Kamasaki T, O'Toole E, Kita S, Osumi M, Usukura J, McIntosh JR, Goshima G. 2013. Augmin-dependent microtubule nucleation at microtubule walls in the spindle. *The Journal of cell biology* **202**:25–33. doi:10.1083/jcb.201304031

Kanki H, Suzuki H, Itohara S. 2006. High-efficiency CAG-FLPe deleter mice in C57BL/6J background. *Experimental animals* **55**:137–141. doi:10.1538/expanim.55.137

Lambrus BG, Daggubati V, Uetake Y, Scott PM, Clutario KM, Sluder G, Holland AJ. 2016. A USP28-53BP1-p53-p21 signaling axis arrests growth after centrosome loss or prolonged mitosis. *The Journal of cell biology* **214**:143–153. doi:10.1083/jcb.201604054

Lambrus BG, Holland AJ. 2017. A New Mode of Mitotic Surveillance. *Trends in cell biology* **27**:314–321. doi:10.1016/j.tcb.2017.01.004

Lancaster MA, Renner M, Martin C-A, Wenzel D, Bicknell LS, Hurles ME, Homfray T, Penninger JM, Jackson AP, Knoblich JA. 2013. Cerebral organoids model human brain development and microcephaly. *Nature* **501**:373–379. doi:10.1038/nature12517

Lawo S, Bashkurov M, Mullin M, Ferreria MG, Kittler R, Habermann B, Tagliaferro A, Poser I, Hutchins JRA, Hegemann B, Pinchev D, Buchholz F, Peters J-M,

766 Hyman AA, Gingras A-C, Pelletier L. 2009. HAUS, the 8-subunit human
767 Augmin complex, regulates centrosome and spindle integrity. *Current biology :*
768 *CB* **19**:816–826. doi:10.1016/j.cub.2009.04.033
769 Lin Y-N, Lee Y-S, Li S-K, Tang TK. 2020. Loss of CPAP in developing mouse brain
770 and its functional implication in human primary microcephaly. *Journal of Cell*
771 *Science* **133**:jcs243592. doi:10.1242/jcs.243592
772 Marjanović M, Sánchez-Huertas C, Terré B, Gómez R, Scheel JF, Pacheco S,
773 Knobel PA, Martínez-Marchal A, Aivio S, Palenzuela L, Wolfrum U, McKinnon
774 PJ, Suja JA, Roig I, Costanzo V, Lüders J, Stracker TH. 2015. CEP63
775 deficiency promotes p53-dependent microcephaly and reveals a role for the
776 centrosome in meiotic recombination. *Nature Communications* **6**:7676.
777 doi:10.1038/ncomms8676
778 Marthiens V, Basto R. 2020. Centrosomes: The good and the bad for brain
779 development. *Biology of the cell / under the auspices of the European Cell*
780 *Biology Organization* **112**:153–172. doi:10.1111/boc.201900090
781 Marthiens V, Rujano MA, Pennetier C, Tessier S, Paul-Gilloteaux P, Basto R. 2013.
782 Centrosome amplification causes microcephaly. *Nature cell biology* **15**:731–
783 740. doi:10.1038/ncb2746
784 McIntyre RE, Lakshminarasimhan Chavali P, Ismail O, Carragher DM, Sanchez-
785 Andrade G, Forment JV, Fu B, Del Castillo Velasco-Herrera M, Edwards A,
786 van der Weyden L, Yang F, Sanger Mouse Genetics Project, Ramirez-Solis R,
787 Estabel J, Gallagher FA, Logan DW, Arends MJ, Tsang SH, Mahajan VB,
788 Scudamore CL, White JK, Jackson SP, Gergely F, Adams DJ. 2012.
789 Disruption of Mouse Cenpj, a Regulator of Centriole Biogenesis, Phenocopies
790 Seckel Syndrome. *PLoS Genet* **8**:e1003022.
791 doi:10.1371/journal.pgen.1003022.s009
792 McKinley KL, Cheeseman IM. 2017. Large-Scale Analysis of CRISPR/Cas9 Cell-
793 Cycle Knockouts Reveals the Diversity of p53-Dependent Responses to Cell-
794 Cycle Defects. *Developmental Cell* **40**:405-420.e2.
795 doi:10.1016/j.devcel.2017.01.012
796 Meireles AM, Fisher KH, Colombié N, Wakefield JG, Ohkura H. 2009. Wac: a new
797 Augmin subunit required for chromosome alignment but not for acentrosomal
798 microtubule assembly in female meiosis. *The Journal of cell biology* **184**:777–
799 784. doi:10.1083/jcb.200811102

800 Meitinger F, Anzola JV, Kaulich M, Richardson A, Stender JD, Benner C, Glass CK,
801 Dowdy SF, Desai A, Shiau AK, Oegema K. 2016. 53BP1 and USP28 mediate
802 p53 activation and G1 arrest after centrosome loss or extended mitotic
803 duration. *The Journal of cell biology* **214**:155–166. doi:10.1083/jcb.201604081
804 Meunier S, Vernos I. 2015. Acentrosomal Microtubule Assembly in Mitosis: The
805 Where, When, and How. *Trends in cell biology*. doi:10.1016/j.tcb.2015.09.001
806 Mitchell-Dick A, Chalem A, Pilaz L-J, Silver DL. 2020. Acute Lengthening of
807 Progenitor Mitosis Influences Progeny Fate during Cortical Development in
808 vivo. *Developmental Neuroscience* 1–18. doi:10.1159/000507113
809 Nano M, Basto R. 2017. Consequences of Centrosome Dysfunction During Brain
810 Development. *Advances in experimental medicine and biology* **1002**:19–45.
811 doi:10.1007/978-3-319-57127-0_2
812 Novorol C, Burkhardt J, Wood KJ, Iqbal A, Roque C, Coutts N, Almeida AD, He J,
813 Wilkinson CJ, Harris WA. 2013. Microcephaly models in the developing
814 zebrafish retinal neuroepithelium point to an underlying defect in metaphase
815 progression. *Open Biol* **3**:130065. doi:10.1098/rsob.130065
816 Petry S. 2016. Mechanisms of Mitotic Spindle Assembly. *Annual review of*
817 *biochemistry* **85**:659–683. doi:10.1146/annurev-biochem-060815-014528
818 Petry S, Groen AC, Ishihara K, Mitchison TJ, Vale RD. 2013. Branching Microtubule
819 Nucleation in Xenopus Egg Extracts Mediated by Augmin and TPX2. *Cell*
820 **152**:768–777. doi:10.1016/j.cell.2012.12.044
821 Phan TP, Maryniak AL, Boatwright CA, Lee J, Atkins A, Tijhuis A, Spierings DC,
822 Bazzi H, Foijer F, Jordan PW, Stracker TH, Holland AJ. 2021. Centrosome
823 defects cause microcephaly by activating the 53BP1-USP28-TP53 mitotic
824 surveillance pathway. *The EMBO Journal* **40**. doi:10.15252/embj.2020106118
825 Pilaz L-J, McMahon JJ, Miller EE, Lennox AL, Suzuki A, Salmon E, Silver DL. 2016.
826 Prolonged Mitosis of Neural Progenitors Alters Cell Fate in the Developing
827 Brain. *Neuron* **89**:83–99. doi:10.1016/j.neuron.2015.12.007
828 Prosser SL, Pelletier L. 2017. Mitotic spindle assembly in animal cells: a fine
829 balancing act. *Nature reviews Molecular cell biology* **18**:187–201.
830 doi:10.1038/nrm.2016.162
831 Quignon F, Rozier L, Lachages A-M, Bieth A, Simili M, Debatisse M. 2007. Sustained
832 mitotic block elicits DNA breaks: one-step alteration of ploidy and

chromosome integrity in mammalian cells. *Oncogene* **26**:165–172. doi:10.1038/sj.onc.1209787

Sánchez-Huertas C, Freixo F, Viais R, Lacasa C, Soriano E, Lüders J. 2016. Non-centrosomal nucleation mediated by augmin organizes microtubules in post-mitotic neurons and controls axonal microtubule polarity. *Nature Communications* **7**:12187. doi:10.1038/ncomms12187

Tariq A, Green L, Jeynes JCG, Soeller C, Wakefield JG. 2020. In vitro reconstitution of branching microtubule nucleation. *eLife* **9**. doi:10.7554/eLife.49769

Taverna E, Götz M, Huttner WB. 2014. The cell biology of neurogenesis: toward an understanding of the development and evolution of the neocortex. *Annual review of cell and developmental biology* **30**:465–502. doi:10.1146/annurev-cellbio-101011-155801

Tronche F, Kellendonk C, Kretz O, Gass P, Anlag K, Orban PC, Bock R, Klein R, Schutz G. 1999. Disruption of the glucocorticoid receptor gene in the nervous system results in reduced anxiety. *Nature genetics* **23**:99–103. doi:10.1038/12703

Uehara R, Nozawa R, Tomioka A, Petry S, Vale RD, Obuse C, Goshima G. 2009. The augmin complex plays a critical role in spindle microtubule generation for mitotic progression and cytokinesis in human cells. *Proceedings of the National Academy of Sciences of the United States of America* **106**:6998–7003. doi:10.1073/pnas.0901587106

Uzquiano A, Gladwyn Ng I, Nguyen L, Reiner O, Götz M, Matsuzaki F, Francis F. 2018. Cortical progenitor biology: key features mediating proliferation versus differentiation. *Journal of neurochemistry* **146**:500–525. doi:10.1111/jnc.14338

Wainman A, Buster DW, Duncan T, Metz J, Ma A, Sharp D, Wakefield JG. 2009. A new Augmin subunit, Msd1, demonstrates the importance of mitotic spindle-templated microtubule nucleation in the absence of functioning centrosomes. *Genes & development* **23**:1876–1881. doi:10.1101/gad.532209

Watanabe S, Shioi G, Furuta Y, Goshima G. 2016. Intra-spindle Microtubule Assembly Regulates Clustering of Microtubule-Organizing Centers during Early Mouse Development. *Cell Reports* **15**:54–60. doi:10.1016/j.celrep.2016.02.087

Zhu H, Coppinger JA, Jang C-Y, Yates JR, Fang G. 2008. FAM29A promotes microtubule amplification via recruitment of the NEDD1-gamma-tubulin

complex to the mitotic spindle. *The Journal of cell biology* **183**:835–848. doi:10.1083/jcb.200807046

Figure 1: Loss of *Haus6* aborts forebrain development.

(a) Schematic representation of the experimental strategy used to evaluate the role of augmin during mouse brain development through generation of brain-specific Nestin-Cre *Haus6* cKO embryos. **(b)** Pictures of E17.5 control (*Haus6*$^{fl/fl}$ Nestin-Cre^{-}) and *Haus6* cKO (*Haus6*$^{fl/fl}$ Nestin-Cre^{+}) embryos. **(c, d)** Coronal histological sections from (**c**) E17.5 and (**d**) E13.5 control and *Haus6* cKO stained with haematoxylin-eosin. Different brain structures are labeled: Ctx (cortex), Tlm (thalamus), Hptlm (hypothalamus), Mb (midbrain), Crbl (cerebellum), MO (medulla oblongata) and CP (choroid plexus). **(e)** Representative images of the cortex (Ctx) and thalamus (Tlm) of E13.5 control (*Haus6*$^{fl/wt}$ Nestin-Cre^{+}) and *Haus6* cKO (*Haus6*$^{fl/fl}$ Nestin-Cre^{+}) embryos. Coronal sections were stained against PAX6 (magenta - apical progenitors) and βIII-tubulin (green - neurons). Yellow arrowheads highlight regions of the thalamus where tissue disruption is observed in *Haus6* cKO embryos. Yellow boxes indicate the regions used for quantifications in (**f**). **(f)** Quantification of the total radial thickness of the thalamus in E13.5 embryos and of layers formed by PAX6- and βIII-tubulin-positive cells. n=3 control and n=5 *Haus6* cKO embryos. Plotted values are means, error bars show SD. **P<0.01, ***P<0.001 by two-tailed t-test. Scale bars: (b) 5 mm, (c) 1 mm, (d) 0.5 mm, (e) 150 μm.

Figure 1-figure supplement 1: Forebrain structures are absent in *Haus6* cKO embryos at E17.5. (a) Schematic representation of the wild type *Haus6* allele (wt), the targeted allele (fl Neo), the floxed *Haus6* allele (fl) and the *Haus6* knockout allele (ko). Positions of exons 1–3, loxP sequences (black triangles), flippase recognition target sequences (FRT) (white triangles) and neomycin resistance cassette (Neo) are shown. Positions of PCR primers are indicated by blue arrows and expected PCR fragments are indicated. **(b)** DNA gels showing genomic PCRs from dissected liver and forebrain of E13.5 embryos with different genotypes. In the upper gel, amplification of a 100 bp fragment using Nestin-Cre recombinase primers indicates the presence of the transgene. In the lower gel, amplification of a 1080, 800 and/or 570 bp fragment reveals the presence of *Haus6* floxed, wild type or knockout alleles, respectively, in the indicated genotypes and tissues. The band that is visible below the 1080 bp band in heterozygous samples is an artefact that results from heteroduplexes of floxed (1080 bp) and wild type (530 bp) DNA strands due to extended regions of complementary. Genomic PCR products were run on a 3% agarose gel. **(c)** Sagittal histological sections from E17.5 control (*Haus6*$^{fl/fl}$ Nestin-Cre^{-}) and *Haus6* cKO (*Haus6*$^{fl/fl}$ Nestin-Cre^{+}) embryos stained with haematoxylin-eosin. Scale bars: (c) 2.5 mm.

Figure 2: Augmin deficiency in neural progenitors impairs mitotic spindle assembly and induces p53 expression and apoptosis.

(a) Representative images of phospho-Histone H3 (pH3) positive mitotic cells in the thalamus of E13.5 control (*Haus6*$^{fl/wt}$ Nestin-Cre^{+}) and *Haus6* cKO (*Haus6*$^{fl/fl}$ Nestin-Cre^{+}) embryos. Staining of pH3 in red and DAPI in blue. **(b)** Quantification of the density of mitotic cells close to the ventricular surface (VS) (<30 µm away) and in outer layers of the cortical plate (>30 µm away). n=4 control and n=4 *Haus6* cKO embryos (total of 203 and 697 mitotic cells, respectively, in 2-4 sections per embryo). **(c)** Quantification of mitotic progenitors at different mitotic stages. n=4 control and n=5 *Haus6* cKO embryos (total of 261 and 427 mitotic cells, respectively, in 1 section per embryo). **(d)** E13.5 control and *Haus6* cKO coronal thalamus sections stained with antibodies against γ-tubulin (green) and DAPI to label DNA (blue). Yellow arrowheads point to γ-tubulin staining at spindle poles. Light blue arrowheads point to spindle-associated γ-tubulin staining. Insets are 1.4x magnifications of spindle poles in the example cells. **(e)** Quantification of the percentage of mitotic cells in (d) with fragmented centrosomes. n=5 control and n=3 *Haus6* cKO embryos (total of 135 and 198 cells counted, respectively, 18-69 cells per embryo). **(f)** Coronal thalamus sections stained with antibodies against α-tubulin (green) and pH3 (blue). **(g)** Quantification of the percentage of mitotic progenitors from control and *Haus6* cKO E13.5 embryos displaying disorganized or no spindles. n=5 Control and n=3 *Haus6* cKO embryos (total of 152 cells and 90 cells counted, respectively, 27-32 cells per embryo). **(h)** Examples of *Haus6* cKO mitotic progenitors in the E13.5 thalamus in which spindle microtubules, stained with anti-α-tubulin antibodies, cannot be detected, whereas spindles are present in control cells. **(i)** Quantification of cells as in (h) without detectable spindle microtubules. n=3 for control and n=4 for *Haus6*

cKO embryos (total of 216 and 243 cells counted, respectively, 40-88 cells per embryo) **(j)** Representative images of control (*Haus6*$^{fl/wt}$ Nestin-Cre^{+}) and *Haus6* cKO (*Haus6*$^{fl/fl}$ Nestin-Cre^{+}) coronal thalamus sections stained with an antibody against p53 (red – upper panel) and the apoptotic marker cleaved caspase-3 (green – lower panel). DNA is labeled with DAPI (blue). **(k)** Quantification of the density of p53- and cleaved caspase-3-positive cells in the E13.5 thalamus in brain sections as shown in (j). n=4 control and n=3 *Haus6* cKO embryos for quantifications of p53 positive cells and n=3 control and n=3 *Haus6* cKO embryos for cleaved caspase-3-positive cells (an area between 460 and 3950 μm^2 quantified per embryo). **(l)** Representative images of *Haus6* cKO coronal brain sections showing the thalamus stained for p53 (red), PAX6 (cyan) and βIII-tubulin (yellow). The inset is a 1.8x magnification of cells with nuclei staining positive for both p53 and PAX6. **(m)** Quantification of the percentage of *Haus6* cKO cells showing induction of p53 and co-expressing PAX6 (orange), βIII-tubulin (light green) or none of these markers (grey). E13.5 thalamus regions, n=3 different *Haus6* cKO embryos (total of 1020 p53-positive cells). **(b, c, e, g, i, k, m)** Plotted values are means, error bars show SD. *P<0.05, **P<0.01, ***P<0.001 by two-tailed t-test. Scale bars: (a) 20 μm, (d, f, h) 3 μm, (j, l) 25 μm.

Figure 2-figure supplement 1: *Haus6* cKO induces mitotic defects in the cortex at E11.5.

(a) Representative images of apical progenitors at different mitotic stages. **(b)** E11.5 control (*Haus6*$^{wt/wt}$ Nestin-Cre^{+}) and *Haus6* cKO cortex (*Haus6*$^{fl/fl}$ Nestin-Cre^{+}) stained with antibodies against the mitotic marker phospho-Histone H3 (red), γ-tubulin (green) and DAPI to label DNA (blue). **(c)** Sections as in (b) were stained with an antibody against βIII-tubulin (green) and DAPI to label DNA (blue). **(d)** Quantification of the density of mitotic cells close to the ventricular surface (<30 µm away) and in outer layers of the cortical plate (>30 µm away). **(e)** Quantification of mitotic stages as in (a) observed in cortical progenitors close to the ventricular surface. **(d, e)** Plots show mean values, error bars indicate SD. n=3 Nestin-Cre control and n=2 Nestin-Cre *Haus6* cKO individual embryos. *P<0.05; **P<0.01 by two-tailed t-test. **(f)** Control and *Haus6* cKO mitotic progenitors in the E13.5 thalamus stained with antibodies against γ-tubulin and centrin and with DAPI to stain DNA. **(g)** Quantification of centrioles (centrin foci) in mitotic cells as in (f). The percentage of cells displaying the indicated number of centrin foci was plotted. n=3 control and n=3 *Haus6* cKO embryos (total of 78 and 114 cells counted, respectively, 19-41 cells per embryo) **(h)** Image illustrating how spindle orientation was quantified based on the angle formed between the spindle axis and the ventricular lining. **(i, j)** Quantification of mitotic spindle angles in progenitors at meta/ana/telophase in E11.5 cortex (i) and E13.5 thalamus (j). Diagrams show the distribution of the spindle angle values between 0º to 90º, grouped in 15º intervals. Each dot represents 1% of the analyzed cells. E11.5 cortex: n=84 control and n=44 *Haus6* cKO mitotic cells from 4 and 2 individual embryos, respectively. E13.5 thalamus: n=85 control and n=113 *Haus6*

974 cKO mitotic cells from 4 and 5 individual embryos, respectively. Scale bars (a, f) 3
975 µm, (b, c) 30 µm, (h) 2.5 µm.
976

Figure 2-figure supplement 2: *Haus6* cKO induces apoptosis and cell cycle arrest.

(a) Sections showing E11.5 control and *Haus6* cKO E11.5 cortex stained with antibodies against p53 (red) and the apoptotic marker cleaved caspase-3 (green). DNA was stained with DAPI. **(b)** Immunohistochemistry sections showing E13.5 thalamus stained with antibodies against p21. n=3 control and n=5 *Haus6* cKO embryos were analyzed. (total of 40460 and 41063 cells per genotype, respectively, 3799-19669 cells in 2-3 sections per embryo) **(c)** The percentage of p21-positive cells was quantified in sections of control and *Haus6* cKO embryos. Plot shows mean values, error bars indicate SD. *p<0.05 by two-tailed t-test. Scale bars: (a, b) 30 μm.

Figure 3: Co-deletion of *Trp53* rescues apoptosis but not abortion of forebrain development.

(a) Schematic overview showing the experimental strategy used to generate *Haus6* cKO *Trp53* KO embryos, to test p53 dependency of the brain development phenotypes observed in *Haus6* cKO embryos. **(b)** Coronal sections of E13.5 control (*Haus6*$^{fl/wt}$ Nestin-Cre^{+}), *Haus6* cKO (*Haus6*$^{fl/fl}$ Nestin-Cre^{+}) and *Haus6* cKO *Trp53* KO (*Haus6*$^{fl/fl}$ Nestin-Cre^{+} *Trp53*$^{-/-}$) embryos stained with haematoxylin-eosin. **(c)** Coronal sections of the thalamus and cortex of E13.5 *Trp53* KO Control and *Haus6* cKO embryos stained against the apoptotic marker cleaved caspase-3 (green). DNA was labeled by DAPI (blue). **(d)** Quantification of the density of cleaved caspase-3 positive cells in the E13.5 thalamus and cortex in brain sections as shown in (c). n=5 control, n=5 *Haus6* cKO, n=4 *Trp53* KO control and n=3 *Haus6* cKO *Trp53* KO embryos for quantifications in the thalamus and n=4 *Trp53* KO control and n=4 Haus6 cKO *Trp53* KO embryos for quantifications in the cortex. Plotted values are means, error bars show SD. *P<0.05, **P<0.01, ***P<0.001 by two-tailed t-test. **(e)** Coronal sections of E17.5 Control and *Haus6* cKO *Trp53* KO embryos stained with haematoxylin-eosin. Scale bars: (b) 0.5 mm; (c) 40 µm, 25 µm (cortex); (e) 2 mm.

Figure 3-figure supplement 1: Expression of p21 in augmin-deficient progenitors is rescued by co-deletion of *Trp53.*

(a) Immunohistochemistry sections showing *Trp53* KO (control) and *Haus6* cKO *Trp53* KO cortex at E13.5 stained with antibodies against p21. **(b)** Quantification of p21-expressing cells as in (a). The percentage of p21-positive cells was plotted. n=3 *Trp53* KO and n=4 *Haus6* cKO *Trp53* KO embryos were analyzed. (total of 40502 and 22555 cells per genotype, respectively, 3577-16763 cells in 3 sections per embryo). **(c)** Immunohistochemistry sections showing *Trp53* KO (control) and *Haus6* cKO *Trp53* KO thalamus at E13.5 stained with antibodies against p21. **(d)** Quantification of p21-expressing cells as in (c). The percentage of p21-positive cells was plotted. n=3 *Trp53* KO embryos and n=3 *Haus6* cKO *Trp53* KO embryos were analyzed. (total of 43072 and 41063 cells per genotype, respectively, 2746-23924 cells in 2-3 sections per embryo). **(b, d)** Plots show mean values, error bars indicate SD. Scale bars: (a, c) 30 μm.

Figure 4: Co-deletion of *Trp53* exacerbates mitotic defects caused by augmin deficiency.

(a, b) Representative coronal sections of the **(a)** cortex and the **(b)** thalamus of E13.5 *Trp53* KO control (*Haus6*$^{fl/wt}$ Nestin-Cre^{-} *Trp53*$^{-/-}$) and *Haus6* cKO *Trp53* KO embryos (*Haus6*$^{fl/fl}$ Nestin-Cre^{+} *Trp53*$^{-/-}$). Sections were stained with phosphorylated Histone H3 antibody (red – mitotic cells) and DAPI to stain DNA (blue). **(c)** Quantification of the density of progenitors undergoing mitosis in the cortex at the indicated distances in µm from the ventricular surface (VS). n=3 *Trp53* KO control and n=2 *Haus6* cKO *Trp53* KO embryos (total of 171 and 485 cells, respectively, from 4 sections per embryo). **(d)** Quantification of mitotic progenitors at the indicated mitotic stages. n=3 *Trp53* KO control and n=2 *Haus6* cKO *Trp53* KO embryos (total of 442 and 443 mitotic cells counted, respectively, 140-248 cells per embryo). (**e**) Examples of normal, bipolar mitotic stages and of stages with multipolar and other abnormal configurations in the cortex of E13.5 control and *Haus6* cKO *Trp53* KO embryos, respectively. Coronal sections were stained with an antibody against γ-tubulin to label spindle poles (red) and DAPI (cyan) to label DNA. **(f)** Quantification of the percentage of metaphase cells displaying aligned chromosomes with bipolar (white) and multipolar (blue) configuration in the cortex of embryos with the indicated genotypes. n=3 *Trp53* KO control and n=2 *Haus6* cKO *Trp53* KO embryos (total of 100 and 97 metaphases counted, respectively, 27-51 metaphases per embryo). **(g)** Quantification of the percentage of normal and abnormal ana/telophases in the cortex of embryos with the indicated genotypes. n=3 *Trp53* KO control and n=2 *Haus6* cKO *Trp53* KO embryos (total of 91 and 33 ana/telophases counted, respectively, 16-34 per embryo). **(h)** Quantification of the nucleus area in interphase PAX6-positive progenitors in the cortex of E13.5 *Trp53* KO control and *Haus6* cKO

Trp53 KO embryos. n=5 *Trp53* KO control and n=4 *Haus6* cKO *Trp53* KO embryos (330-2012 nuclei per embryo). **(i)** Quantification of the percentage of metaphase cells displaying aligned chromosomes with multipolar configuration in the thalamus of embryos with the indicated genotypes. n=4 *Trp53* KO control and n=3 *Haus6* cKO *Trp53* KO embryos (total of 156 and 161 metaphases counted, respectively, 32-81 per embryo). **(j)** Quantification of the percentage of abnormal ana/telophases in the thalamus of embryos with the indicated genotypes. n=4 *Trp53* KO control and n=3 *Haus6* cKO *Trp53* KO embryos (total of 103 and 90 ana/telophases counted, respectively, 17-39 per embryo). **(c, d, f, g, h, l, j)** Plots show mean values, error bars indicate SD. *P<0.05, **P<0.01, ***P<0.001 by two-tailed t-test. Scale bars: (a, b) 50 μm (e) 5 μm.

Figure 4-figure supplement 1: Spindle defects persist in *Haus6* cKO *Trp53* KO cells.

(a) E13.5 control and *Haus6* cKO *Trp53* KO coronal cortex sections stained with antibodies against γ-tubulin (green) and DAPI to label DNA (blue). Yellow arrowheads point to γ-tubulin staining at spindle poles. Light blue arrowheads point to spindle-associated γ-tubulin staining. Insets are 1.5x magnifications of spindle poles in the example cells. **(b)** Quantification of the percentage of mitotic cells in (a) with fragmented centrosomes. n=4 *Trp53* KO and n=3 *Haus6* cKO *Trp53* KO embryos (total of 215 and 254 cells counted, respectively, 30-129 cells per embryo). **(c)** Coronal cortex sections from control and *Haus6* cKO *Trp53* KO E13.5 embryos stained with antibodies against α-tubulin (green) to reveal spindle microtubules and DAPI to stain DNA (blue). **(d)** Quantification of the percentage of mitotic progenitors in (c) displaying disorganized spindles. n=4 *Trp53* KO and n=3 *Haus6* cKO *Trp53* KO embryos (total of 215 and 254 cells counted, respectively, 30-129 cells per embryo). **(e)** Sections as in (c) were stained with antibodies against γ-tubulin and centrin, and with DAPI to stain DNA. Note that control and *Haus6* cKO *Trp53* KO cells are shown at different scales due to the increased size of *Haus6* cKO *Trp53* KO cells with extra centrosomes. **(f)** Quantification of the number of centrioles (centrin foci) at spindle poles in mitotic cells as in (e). The percentage of cells with the indicated number of centrioles was plotted. n=3 *Trp53* KO and n=3 *Haus6* cKO *Trp53* KO embryos (total of 82 and 125 cells counted, respectively, 25-62 cells per embryo). **(g)** For the two categories of cells in (f) that have 3-4 or more than 4 centrin foci, respectively, the area occupied by the cells was measured and means were plotted. Total of 62 and 60 mitotic cells, respectively, in n=3 *Trp53* KO *Haus6c*KO embryos. **(b, d, f, g)**

1085 Plotted values are means, error bars show SD. *P<0.05, **P<0.01, ***P<0.001 by
1086 two-tailed t-test. Scale bars: (a,c,e) 3 μm.

Figure 5: Impaired mitosis in augmin-deficient progenitors causes DNA damage.

(a) Representative images of a region of the cortex of E13.5 *Trp53* KO control (*Haus6*$^{fl/wt}$ Nestin-Cre^{+} *Trp53*$^{-/-}$) and *Haus6* cKO *Trp53* KO (*Haus6*$^{fl/fl}$ Nestin-Cre^{+} *Trp53*$^{-/-}$) embryos. Coronal sections were stained by IHC with an antibody against γH2AX (brown). **(b)** Quantification of the percentage of cells overexpressing γH2AX in the E13.5 cortex**.** n=4 embryos for *Trp53* KO control and n=4 embryos for *Haus6* cKO *Trp53* KO (total of 9874 and 14506 cells counted, respectively, 2 sections per embryo). **(c)** Representative images of the region of the thalamus of E13.5 control (*Haus6*$^{fl/wt}$ Nestin-Cre^{+} *Trp53*$^{+/+}$), *Haus6* cKO (*Haus6*$^{fl/fl}$ Nestin-Cre^{+} *Trp53*$^{+/+}$), *Trp53* KO control and *Haus6* cKO *Trp53* KO embryos. **(d)** Quantification of γH2AX-positive cells in the E13.5 thalamus in embryos of the indicated genotypes. n=3 embryos for control, n=4 embryos for *Haus6* cKO, n=4 embryos for *Trp53* KO and n=3 embryos for *Haus6* cKO *Trp53* KO genotypes. (total of 10773, 5433, 23384, 20602 cells counted, respectively, 2 sections per embryo). **(b, d)** Plots show mean values, error bars indicate SD. *P<0.05, **P<0.01, ***P<0.001 by two-tailed t-test. Scale bars: (a, c) 45 µm.

Figure 6: The production of neurons is reduced in *Haus6* cKO and *Haus6* cKO *Trp53* KO brains.

(a) Schematic depicting the experimental procedure of BrdU injection and analysis. **(b)** Examples or brain sections stained with antibodies against BrdU and the proliferation marker Ki67. Identification of BrdU-labeled cells that did not display Ki67 staining is shown. **(c)** Examples or brain sections stained with antibodies against BrdU, the progenitor marker PAX6 and the neuronal marker βIII-tubulin. Identification of BrdU-labeled cells that did not express PAX6 but were positive for βIII-tubulin is shown. **(d)** Quantifications of cells in E13.5 cortex of *Trp53* KO (control) and *Haus6* cKO *Trp53* KO embryos stained as in (b) and (c). The percentage of BrdU-positive cells showing the indicated staining was plotted. For cell cycle exit analysis n=4 *Trp53* KO embryos and n=4 *Haus6* cKO *Trp53* KO embryos were analyzed. (total of 8730 and 7361 BrdU positive cells per genotype, respectively, 1381-2942 cells in 2-3 sections per embryo). For analysis of neurogenesis n=4 *Trp53* KO embryos and n=3 *Haus6* cKO *Trp53* KO embryos were analyzed. (total of 13194 and 8139 BrdU positive cells per genotype, respectively, 1750-4614 in 3-6 sections per embryo). **(e)** Quantifications of cells in E13.5 thalamus of control and *Haus6* cKO, and *Trp53* KO (control) and *Haus6* cKO *Trp53* KO embryos stained as in (b) and (c). The percentage of BrdU-positive cells showing the indicated staining was plotted. For cell cycle exit analysis n=3 control embryos, n=3 *Haus6* cKO embryos, n=4 *Trp53* KO embryos and n=4 *Haus6* cKO *Trp53* KO embryos were analyzed. (total 9050, 5923, 12663, 8610 of BrdU positive cells per genotype, respectively, 1159-4106 cells in 2-3 sections per embryo). For analysis of neurogenesis n=3 control embryos, n=3 *Haus6* cKO embryos, n=4 *Trp53* KO embryos and n=3 *Haus6* cKO *Trp53* KO embryos were analyzed. (total of 11749, 5301, 8927 and 4377 BrdU positive cells per genotype,

1131 respectively, 1363-5087 cells in 2-5 sections per embryo). Plots show mean values,
1132 error bars indicate SD. *P<0.05, **P<0.01, ***P<0.001 by two-tailed t-test. Scale
1133 bars: (b), (c) 40 μm.
1134

Figure 7: Co-deletion of *Haus6* and *Trp53* leads to loss of cortical layering.

(a, b) Representative images of the E13.5 cortex from Trp53 KO control (*Haus6*$^{fl/wt}$ Nestin-Cre^{+} *Trp53*$^{-/-}$) and *Haus6* cKO *Trp53* KO (*Haus6*$^{fl/fl}$ Nestin-Cre^{+} *Trp53*$^{-/-}$) embryos stained with antibodies against PAX6 (a) or TBR2 (b) (red) and the neuronal marker βIII-tubulin (green). DNA was stained with DAPI. **(c)** Representative images of E13.5 cortex from control (*Haus6*$^{fl/fl}$ Nestin-Cre^{-} *Trp53*$^{-/-}$) and *Haus6* cKO *Trp53* KO (*Haus6*$^{fl/fl}$ Nestin-Cre^{+} *Trp53*$^{-/-}$) embryos. Coronal sections were co-stained with antibodies against γ-tubulin (green) and PAX6 (red). DNA was stained with DAPI. Magnifications of the boxed regions labeled with 1, 2, 3 and 4 are shown. In the magnified region labeled with 4, yellow arrowheads point to ectopic clusters of interphase centrosomes. **(d, e)** Distribution of PAX6 and TBR2 staining in sections as in (a) and (b), respectively. Intensity values were averaged into 9,8 µm-thick bins and plotted as percentage of total intensity. Lines connect mean values and error bars display SD. (d) n=5 *Trp53* KO and n=4 *Haus6* cKO *Trp53* KO embryos. (e) n=2 *Trp53* KO and n=2 *Haus6* cKO *Trp53* KO embryos. **(f)** Quantification of the density of centrosome number at the ventricular surface of the cortex of E13.5 *Trp53* KO and *Haus6* cKO *Trp53* KO embryos. n=4 *Trp53* KO and n=4 *Haus6* cKO *Trp53* KO embryos. Plots show mean values and error bars display SD. ***P<0.001 by two-tailed t-test. Scale bars: (a, b) 35 µm; (c) white – 25 µm, yellow – 5 µm.

Figure 7-figure supplement 1: Identification of interphase centrosome clusters in *Haus6* cKO *Trp53* KO cortex.

E13.5 cortical sections were stained with antibodies against γ-tubulin and the centriolar marker centrin. Two regions containing multiple, clustered interphase centrosomes are shown as magnifications. Scale bars: 5 μm and 2 μm (magnifications).

Figure 7-figure supplement 2: Co-deletion of *Haus6* and *Trp53* disrupts polarity in surviving progenitors.

(a) Representative images of E13.5 cortical sections from *Trp53* KO control (*Haus6*$^{fl/fl}$ Nestin-Cre^{-} *Trp53*$^{-/-}$) and *Haus6* cKO (*Haus6*$^{fl/fl}$ Nestin-Cre^{+} *Trp53*$^{-/-}$) embryos stained with antibodies against the apical progenitor marker nestin (red/white) and acetylated α-tubulin, a marker for stable microtubules (green). **(b)** Representative images of E13.5 cortical sections from *Trp53* KO control (*Haus6*$^{fl/fl}$ Nestin-Cre^{-} *Trp53*$^{-/-}$) and *Haus6* cKO *Trp53* KO (*Haus6*$^{fl/fl}$ Nestin-Cre^{+} *Trp53*$^{-/-}$) embryos stained with antibodies against α-tubulin (green/white) and the apical progenitor marker PAX6 (red). **(c)** Magnification of the apical region of the cortex of E13.5 *Trp53* KO control and *Haus6* KO *Trp53* KO embryos showing microtubules stained with α-tubulin antibody. Scale bars: (a) 25 μm, (b) 35 μm, (c) 15 μm.

Figure 1

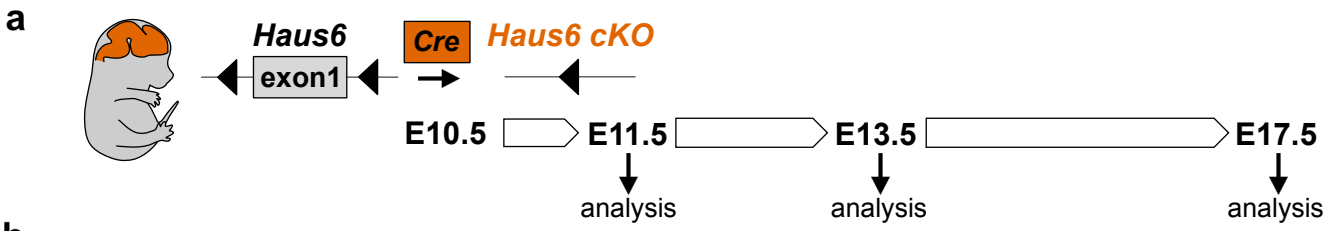
a
Haus6
exon1
Cre
Haus6 cKO
E10.5
E11.5
E13.5
E17.5
analysis
analysis
analysis

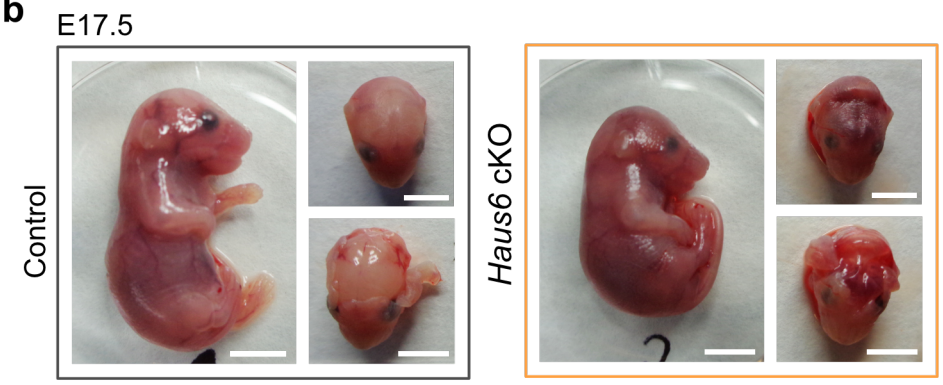
b
E17.5
Control
Haus6 cKO

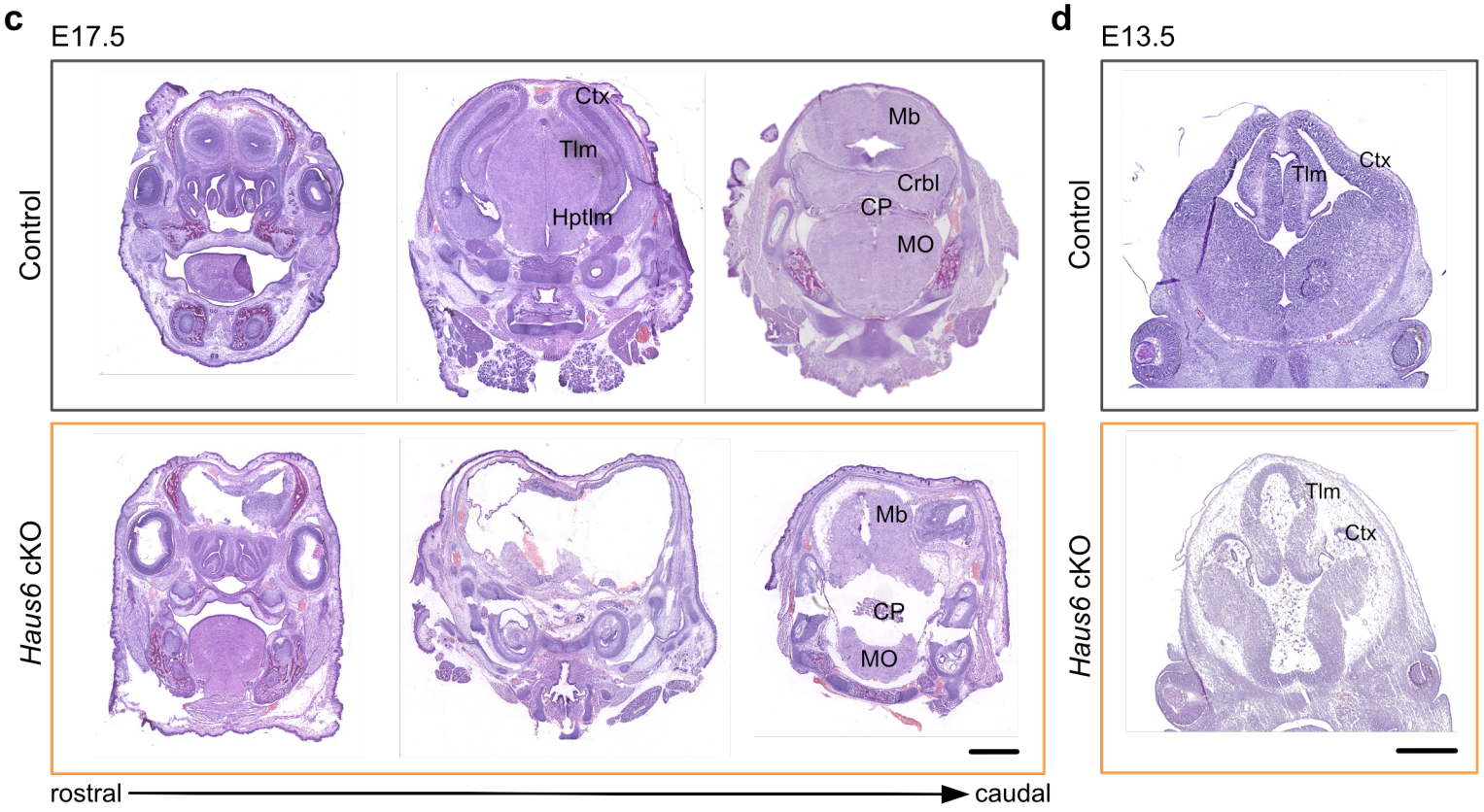
c
E17.5
Control
Haus6 cKO
Ctx
Tlm
Hptlm
Mb
Crbl
CP
MO
d
E13.5
Control
Haus6 cKO
Tlm
Ctx
rostral
caudal

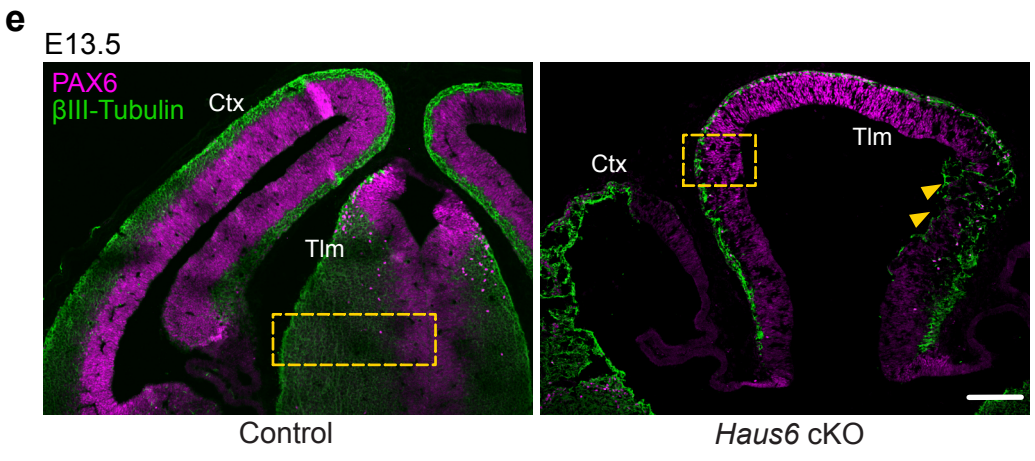
e
E13.5
PAX6
βIII-Tubulin
Ctx
Tlm
Control
Haus6 cKO

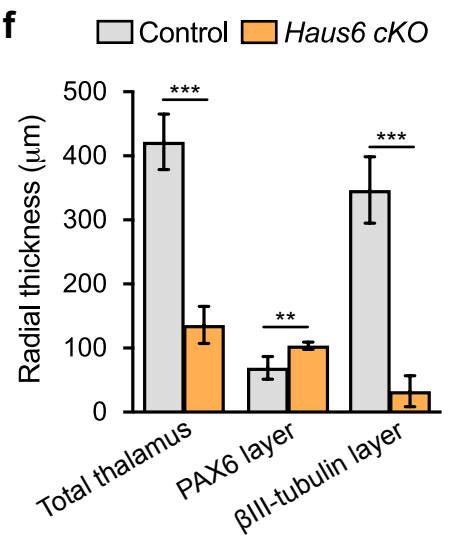
f
Control
Haus6 cKO
Radial thickness (μm)
500
400
300
200
100
0
***
**
***
Total thalamus
PAX6 layer
βIII-tubulin layer

Figure 1-figure supplement 1

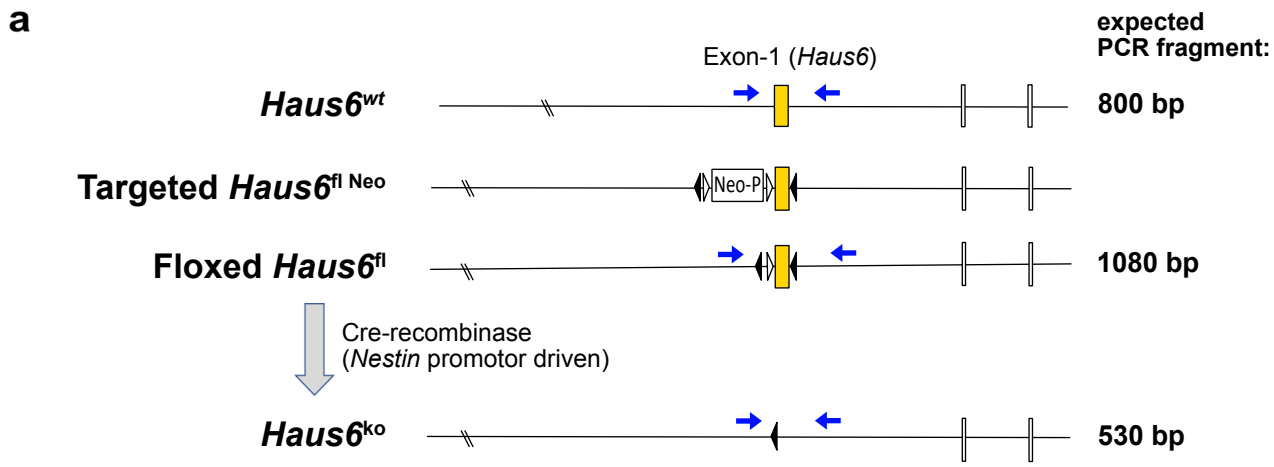

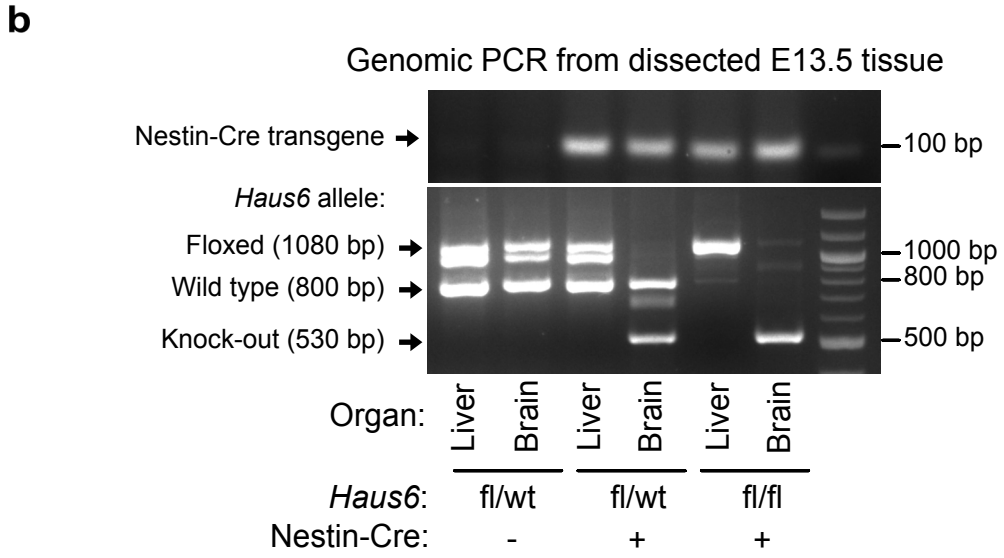

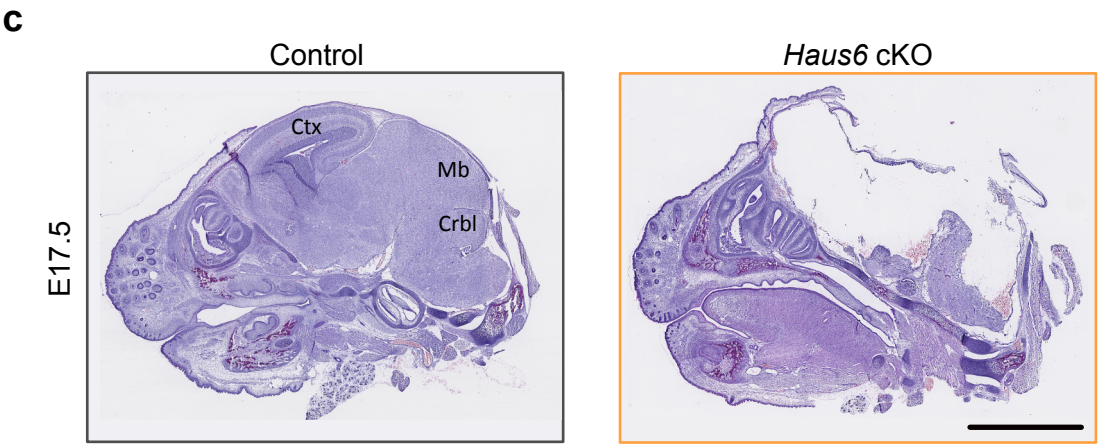

Figure 2

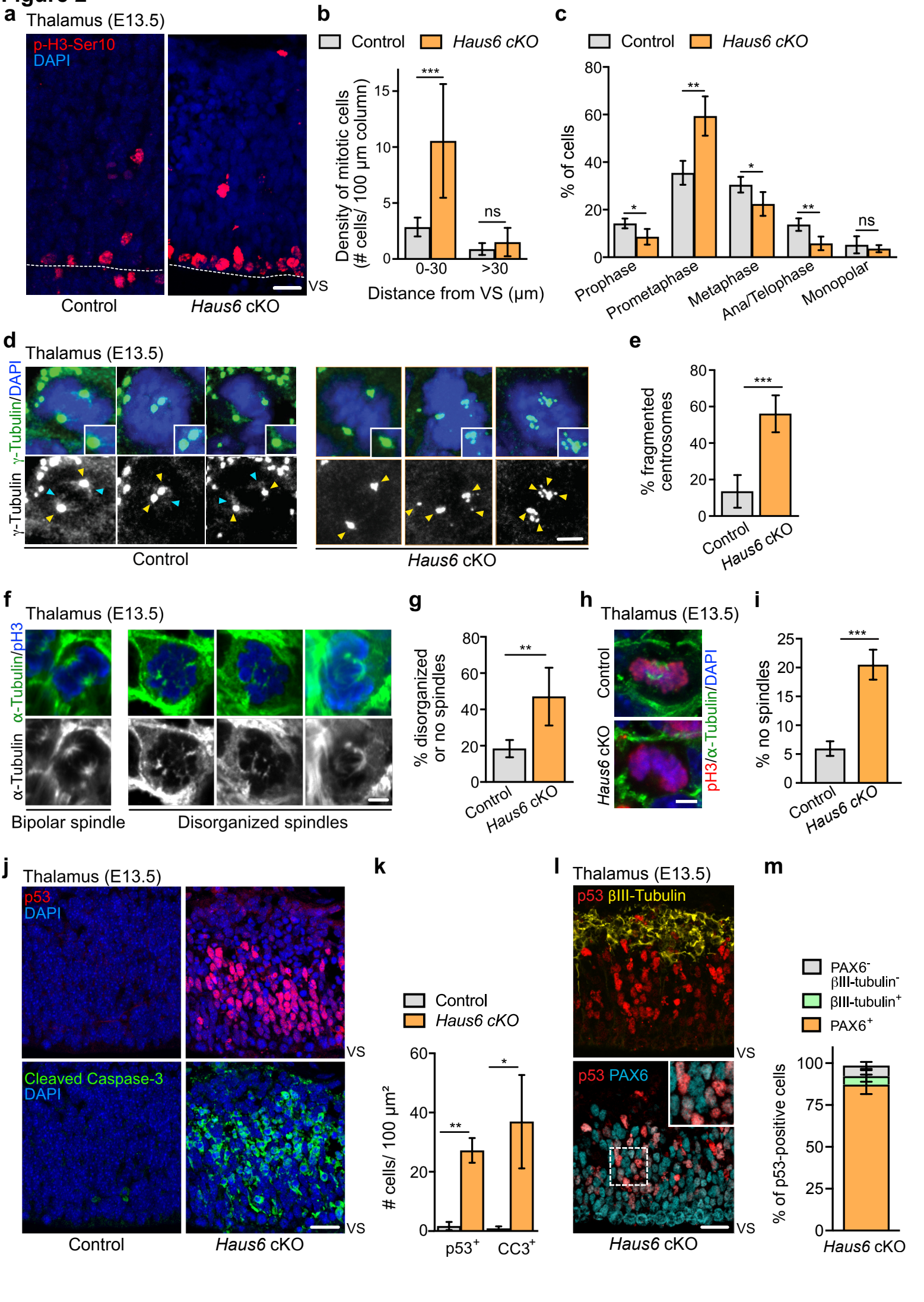
a
Thalamus (E13.5)
p-H3-Ser10
DAPI
VS
Control
Haus6 cKO
b
Control
Haus6 cKO
***
ns
Density of mitotic cells (# cells/ 100 µm column)
0-30
>30
Distance from VS (µm)
c
Control
Haus6 cKO
**
*
*
**
ns
% of cells
Prophase
Prometaphase
Metaphase
Ana/Telophase
Monopolar
d
Thalamus (E13.5)
γ-Tubulin/DAPI
γ-Tubulin
Control
Haus6 cKO
e
***
% fragmented centrosomes
Control
Haus6 cKO
f
Thalamus (E13.5)
α-Tubulin/pH3
α-Tubulin
Bipolar spindle
Disorganized spindles
g
**
% disorganized or no spindles
Control
Haus6 cKO
h
Thalamus (E13.5)
Control
Haus6 cKO
pH3/α-Tubulin/DAPI
i
***
% no spindles
Control
Haus6 cKO
j
Thalamus (E13.5)
p53
DAPI
Cleaved Caspase-3
DAPI
VS
Control
Haus6 cKO
k
Control
Haus6 cKO
**
*
cells/ 100 µm²
p53+
CC3+
l
Thalamus (E13.5)
p53 βIII-Tubulin
p53 PAX6
VS
Haus6 cKO
m
PAX6- βIII-tubulin-
βIII-tubulin+
PAX6+
% of p53-positive cells
Haus6 cKO

Figure 2-figure supplement 1

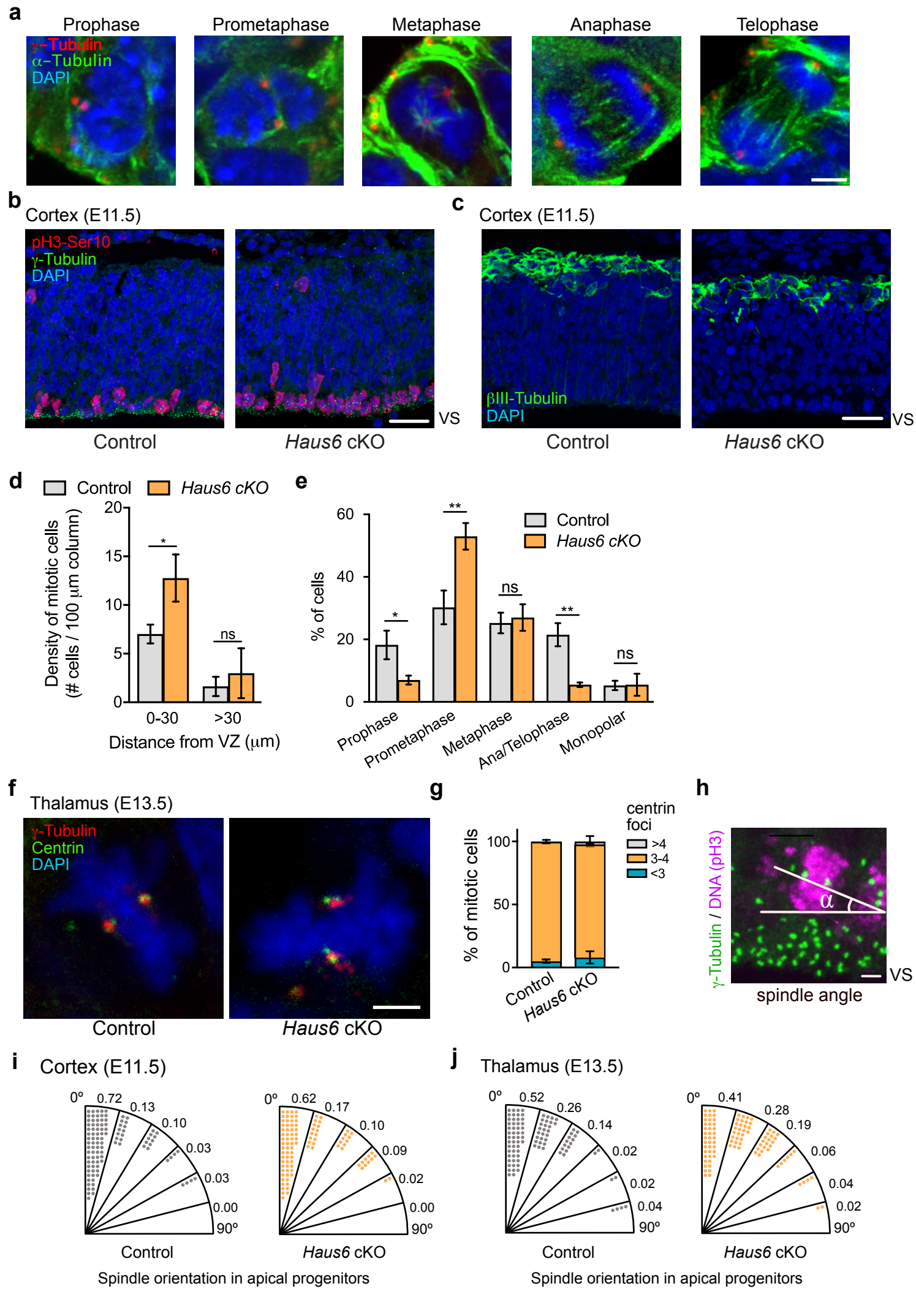

Figure 2-figure supplement 2

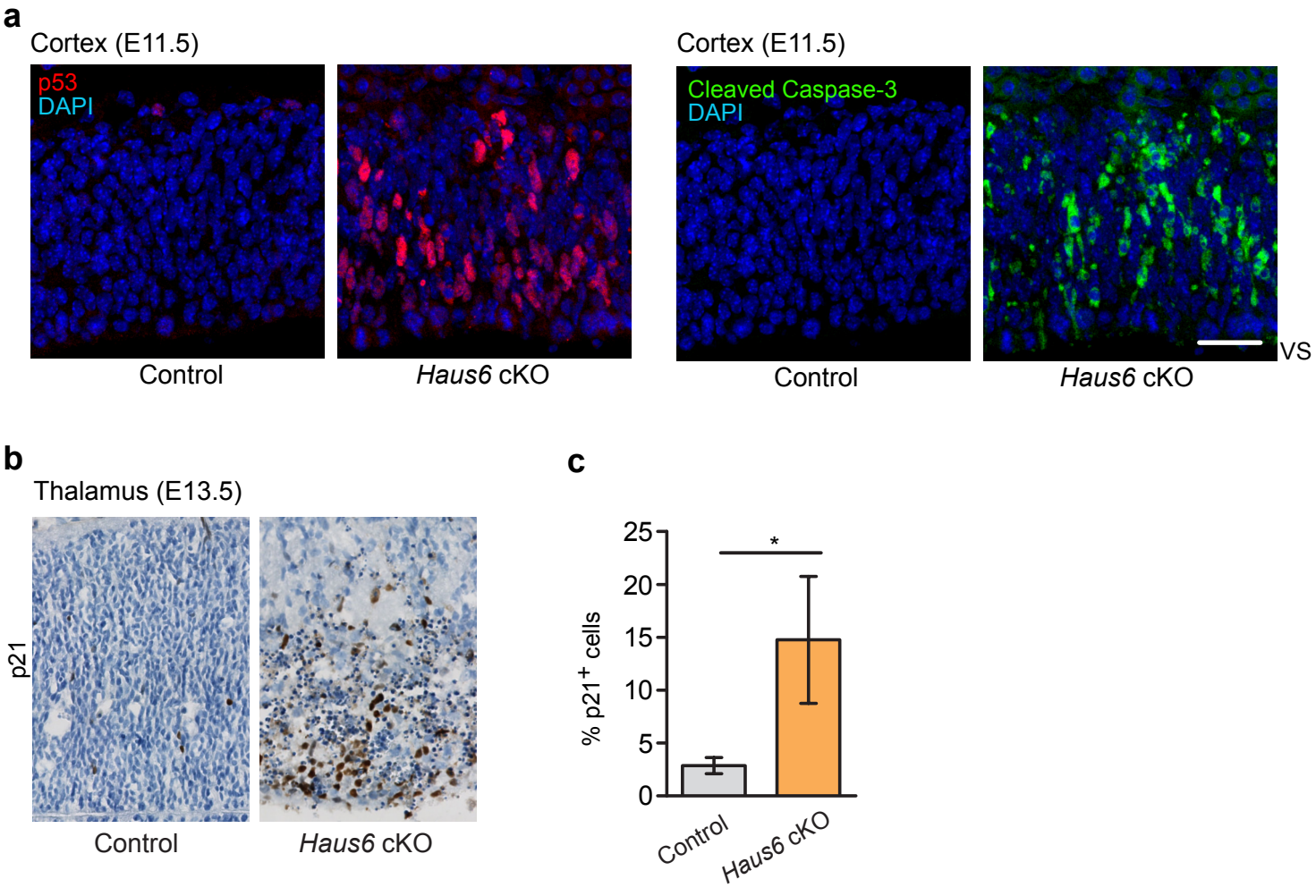

Figure 3

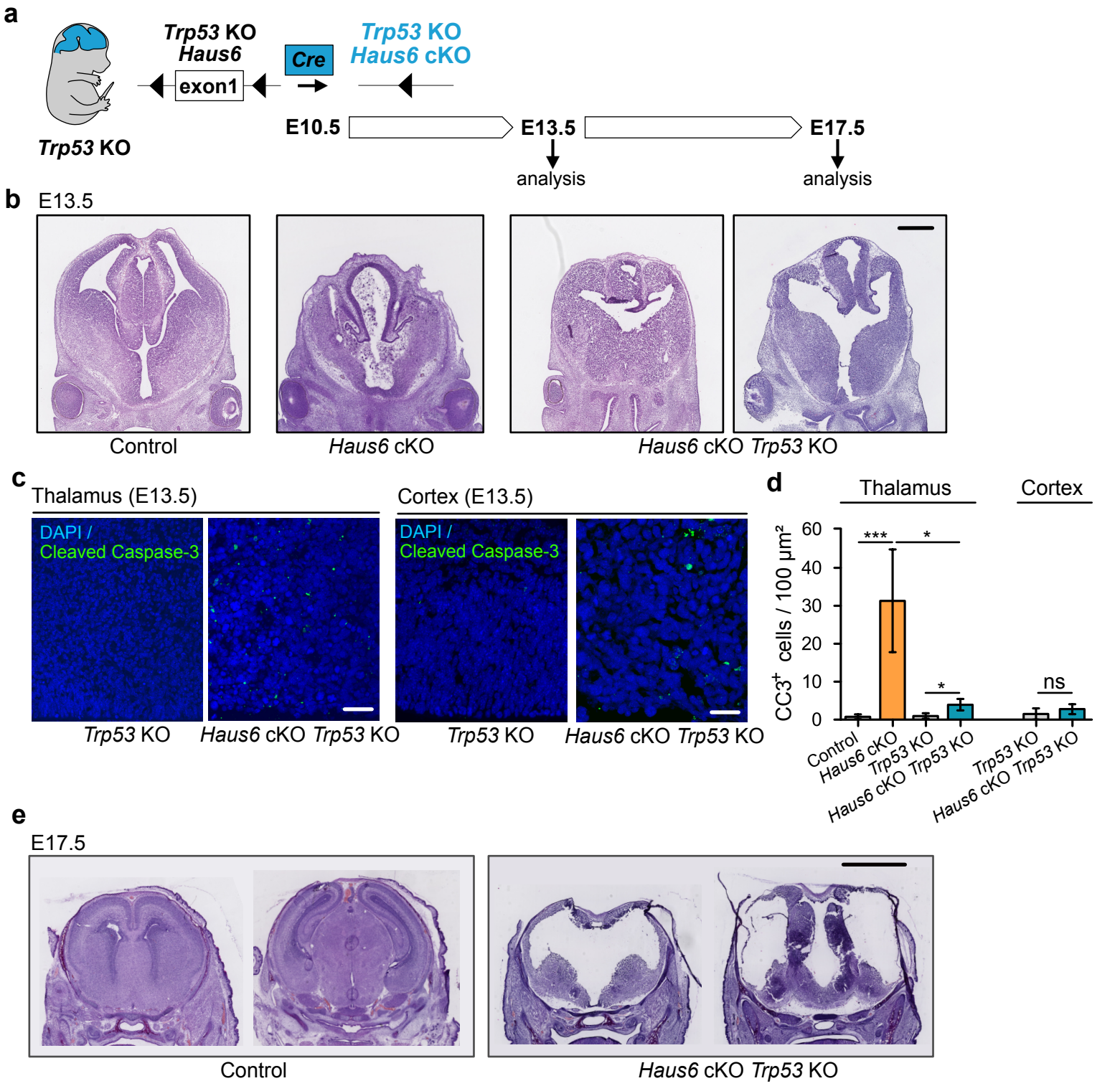
a
Trp53 KO
Haus6
exon1
Cre
Trp53 KO
Haus6 cKO
Trp53 KO
E10.5
E13.5
analysis
E17.5
analysis
b
E13.5
Control
Haus6 cKO
Haus6 cKO Trp53 KO
c
Thalamus (E13.5)
Cortex (E13.5)
DAPI /
Cleaved Caspase-3
Trp53 KO
Haus6 cKO Trp53 KO
Trp53 KO
Haus6 cKO Trp53 KO
d
Thalamus
Cortex
CC3+ cells / 100 µm²
60
40
30
20
10
0
***
*
*
ns
Control
Haus6 cKO
Trp53 KO
Haus6 cKO Trp53 KO
Trp53 KO
Haus6 cKO Trp53 KO
e
E17.5
Control
Haus6 cKO Trp53 KO

Figure 3-figure supplement 1

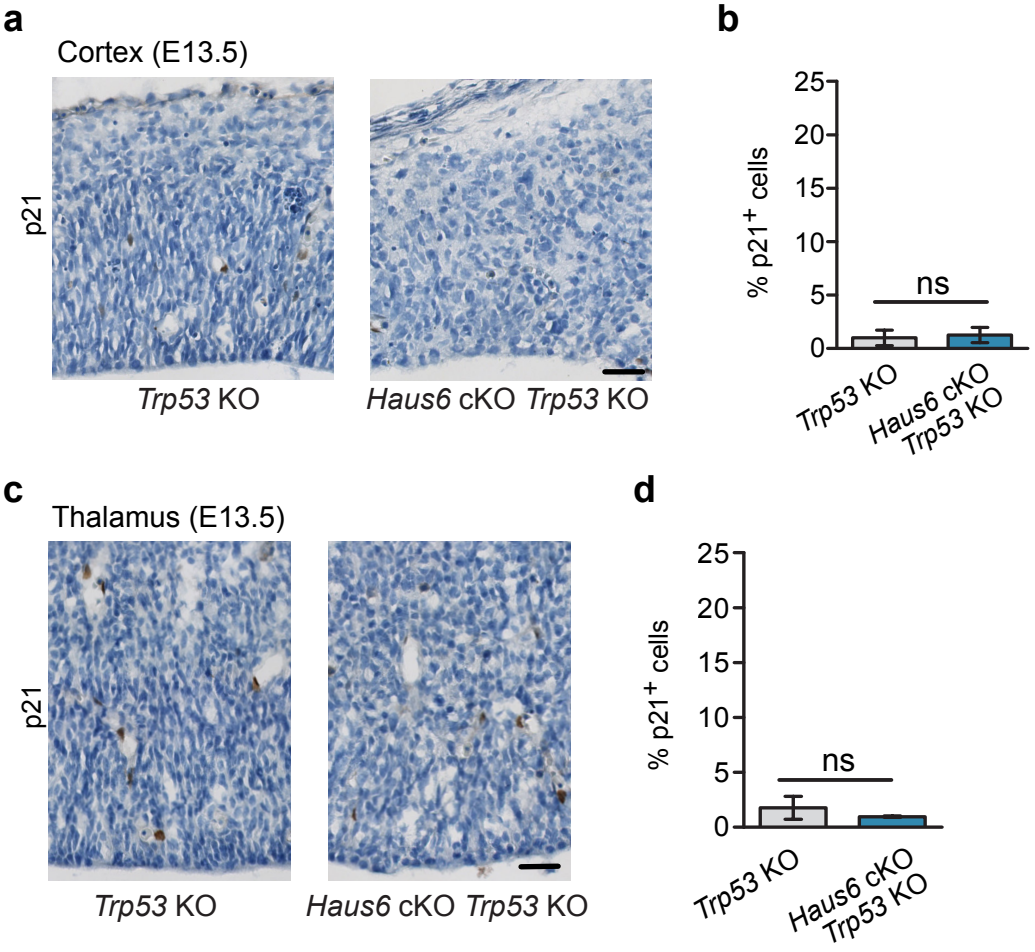

Figure 4

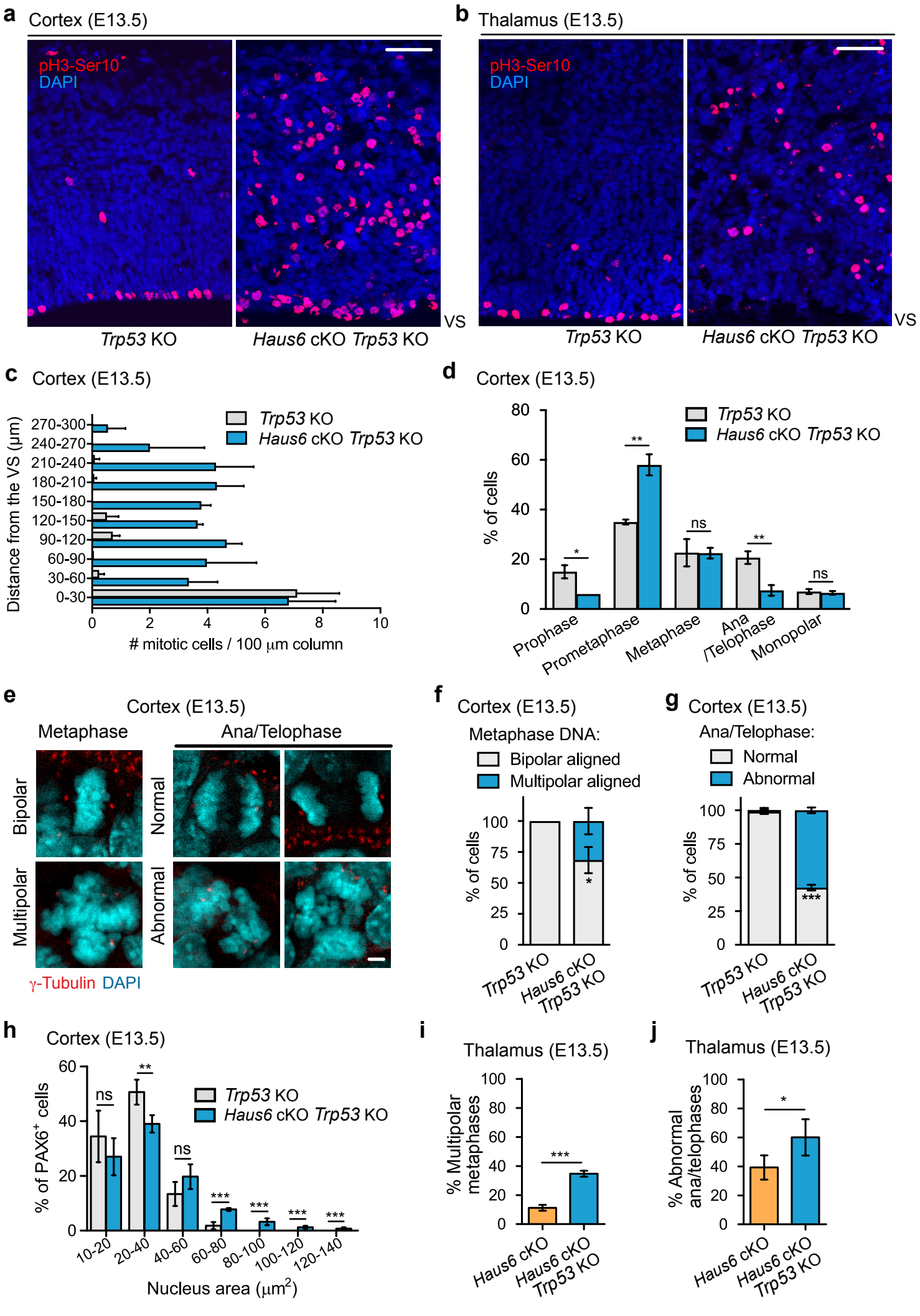
a
Cortex (E13.5)
pH3-Ser10
DAPI
Trp53 KO
Haus6 cKO Trp53 KO
VS
b
Thalamus (E13.5)
pH3-Ser10
DAPI
Trp53 KO
Haus6 cKO Trp53 KO
VS
c
Cortex (E13.5)
Trp53 KO
Haus6 cKO Trp53 KO
Distance from the VS (µm)
270-300
240-270
210-240
180-210
150-180
120-150
90-120
60-90
30-60
0-30
0
2
4
6
8
10
mitotic cells / 100 µm column
d
Cortex (E13.5)
Trp53 KO
Haus6 cKO Trp53 KO
% of cells
80
60
40
20
0
*
**
ns
**
ns
Prophase
Prometaphase
Metaphase
Ana /Telophase
Monopolar
e
Cortex (E13.5)
Metaphase
Ana/Telophase
Bipolar
Multipolar
Normal
Abnormal
γ-Tubulin DAPI
f
Cortex (E13.5)
Metaphase DNA:
Bipolar aligned
Multipolar aligned
% of cells
100
75
50
25
0
*
Trp53 KO
Haus6 cKO Trp53 KO
g
Cortex (E13.5)
Ana/Telophase:
Normal
Abnormal
% of cells
100
75
50
25
0
***
Trp53 KO
Haus6 cKO Trp53 KO
h
Cortex (E13.5)
Trp53 KO
Haus6 cKO Trp53 KO
% of PAX6+ cells
60
40
20
0
ns
**
ns
***
***
***
***
10-20
20-40
40-60
60-80
80-100
100-120
120-140
Nucleus area (µm2)
i
Thalamus (E13.5)
% Multipolar metaphases
100
80
60
40
20
0
***
Haus6 cKO
Haus6 cKO Trp53 KO
j
Thalamus (E13.5)
% Abnormal ana/telophases
100
80
60
40
20
0
*
Haus6 cKO
Haus6 cKO Trp53 KO

Figure 4-figure supplement 1

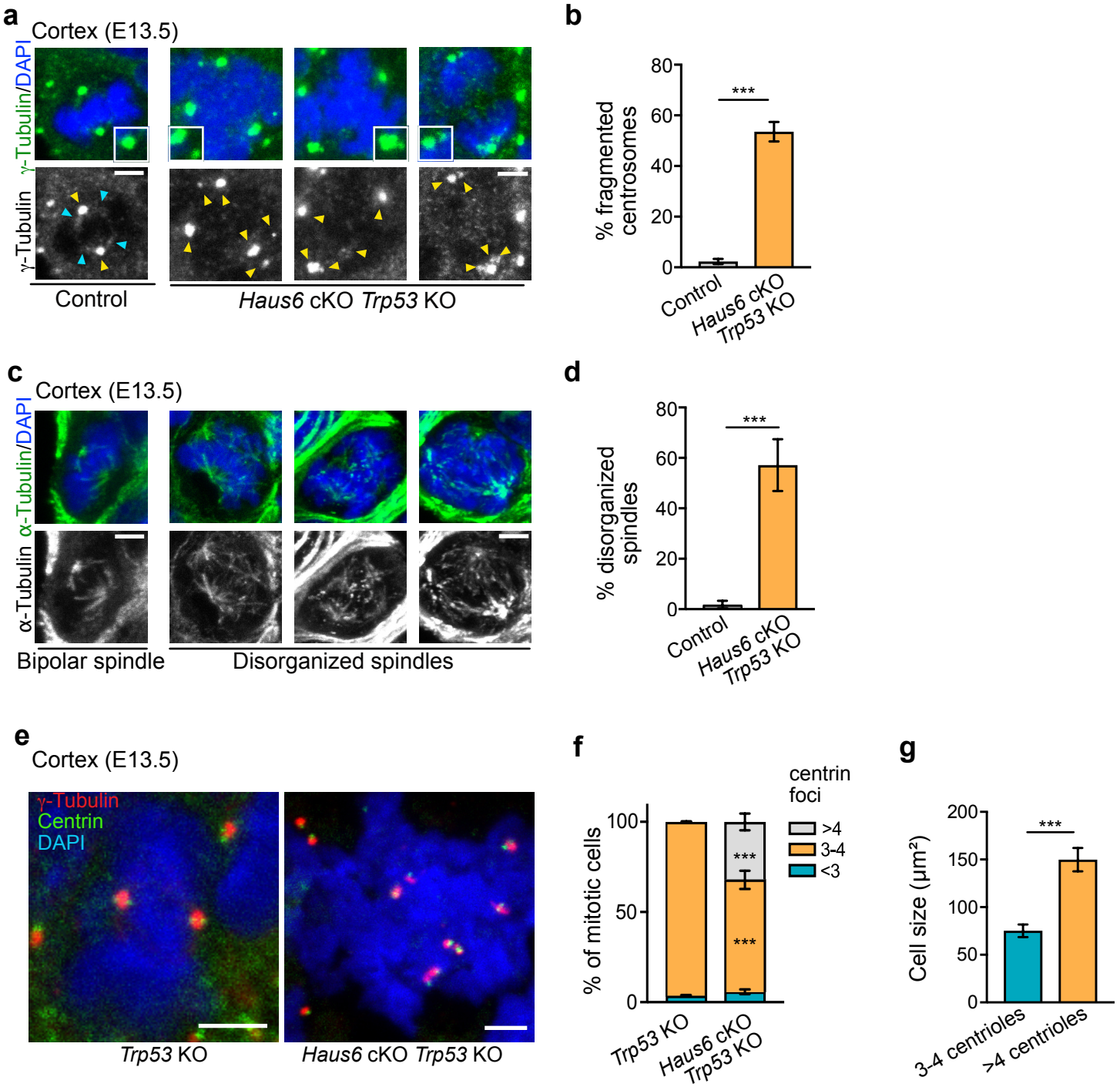

Figure 5

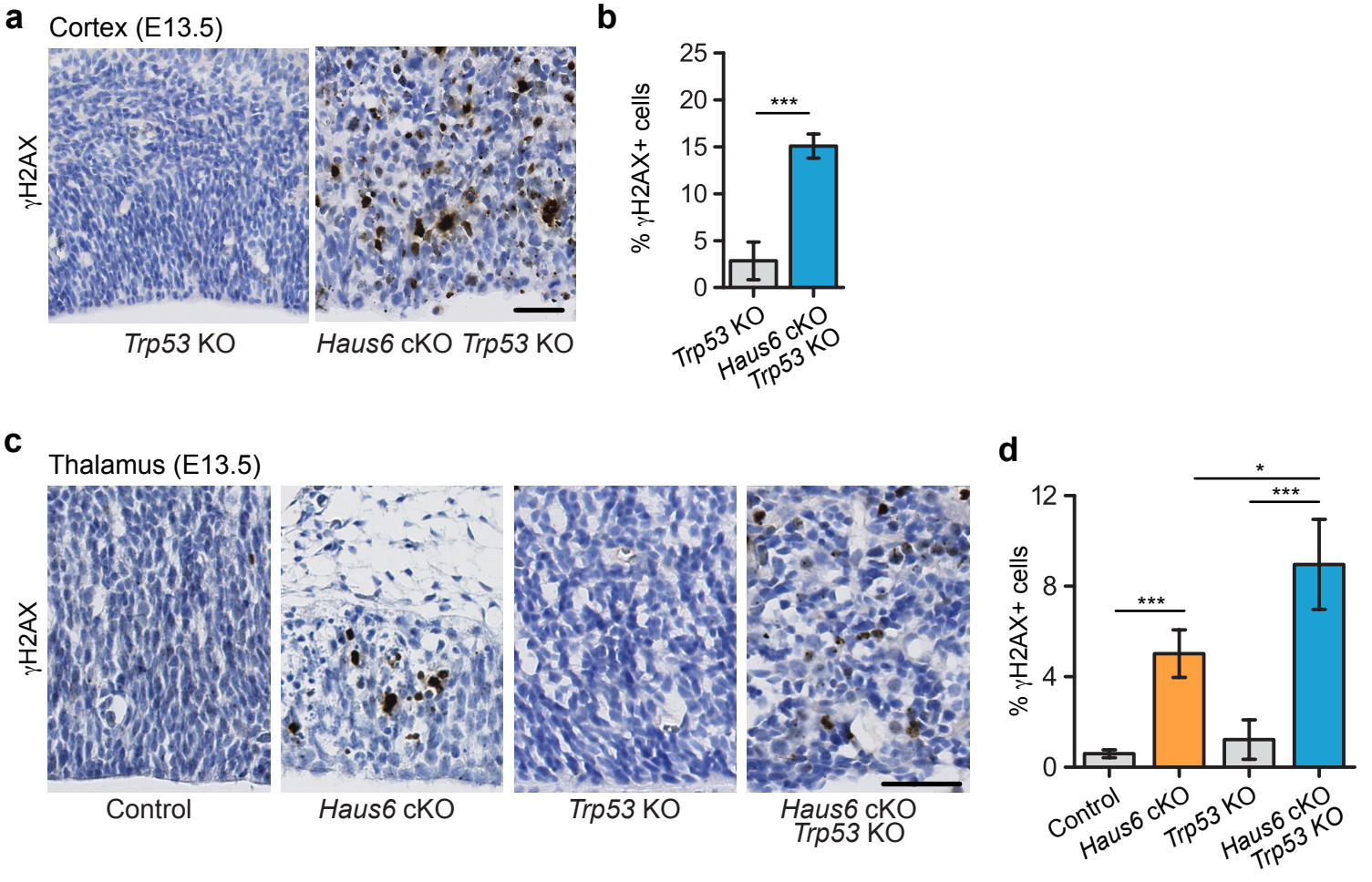
a
Cortex (E13.5)
γH2AX
Trp53 KO
Haus6 cKO Trp53 KO
b
% γH2AX+ cells
25
20
15
10
5
0
***
Trp53 KO
Haus6 cKO Trp53 KO
c
Thalamus (E13.5)
γH2AX
Control
Haus6 cKO
Trp53 KO
Haus6 cKO Trp53 KO
d
% γH2AX+ cells
12
8
4
0
*
***
***
Control
Haus6 cKO
Trp53 KO
Haus6 cKO Trp53 KO

Figure 6

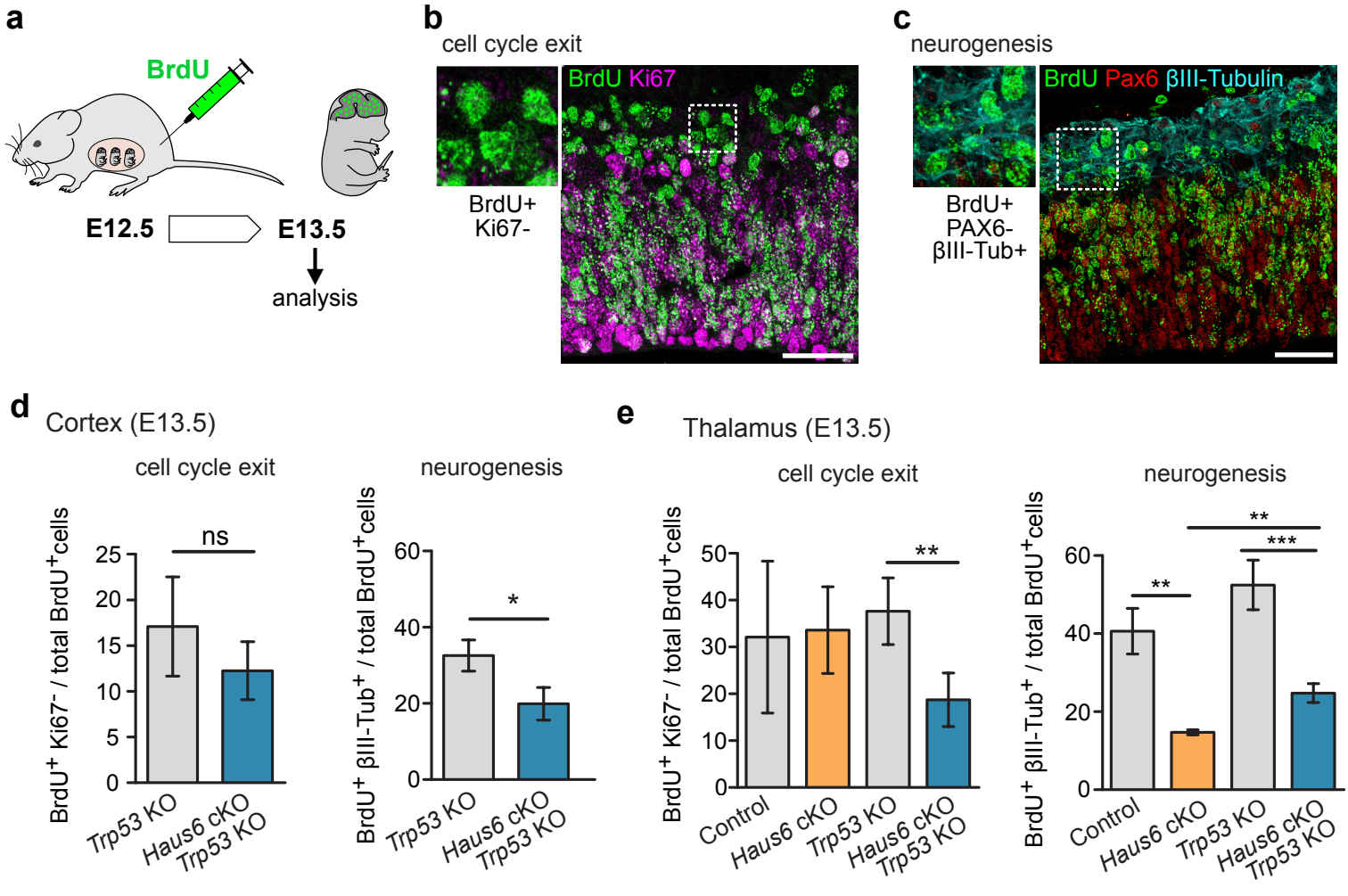
a
BrdU
E12.5
E13.5
analysis
b
cell cycle exit
BrdU Ki67
BrdU+
Ki67-
c
neurogenesis
BrdU Pax6 βIII-Tubulin
BrdU+
PAX6-
βIII-Tub+
d
Cortex (E13.5)
cell cycle exit
neurogenesis
BrdU+ Ki67- / total BrdU+cells
BrdU+ βIII-Tub+ / total BrdU+cells
ns
*
Trp53 KO
Haus6 cKO
Trp53 KO
e
Thalamus (E13.5)
cell cycle exit
neurogenesis
**
**
***
Control
Haus6 cKO
Trp53 KO
Haus6 cKO
Trp53 KO

Figure 7

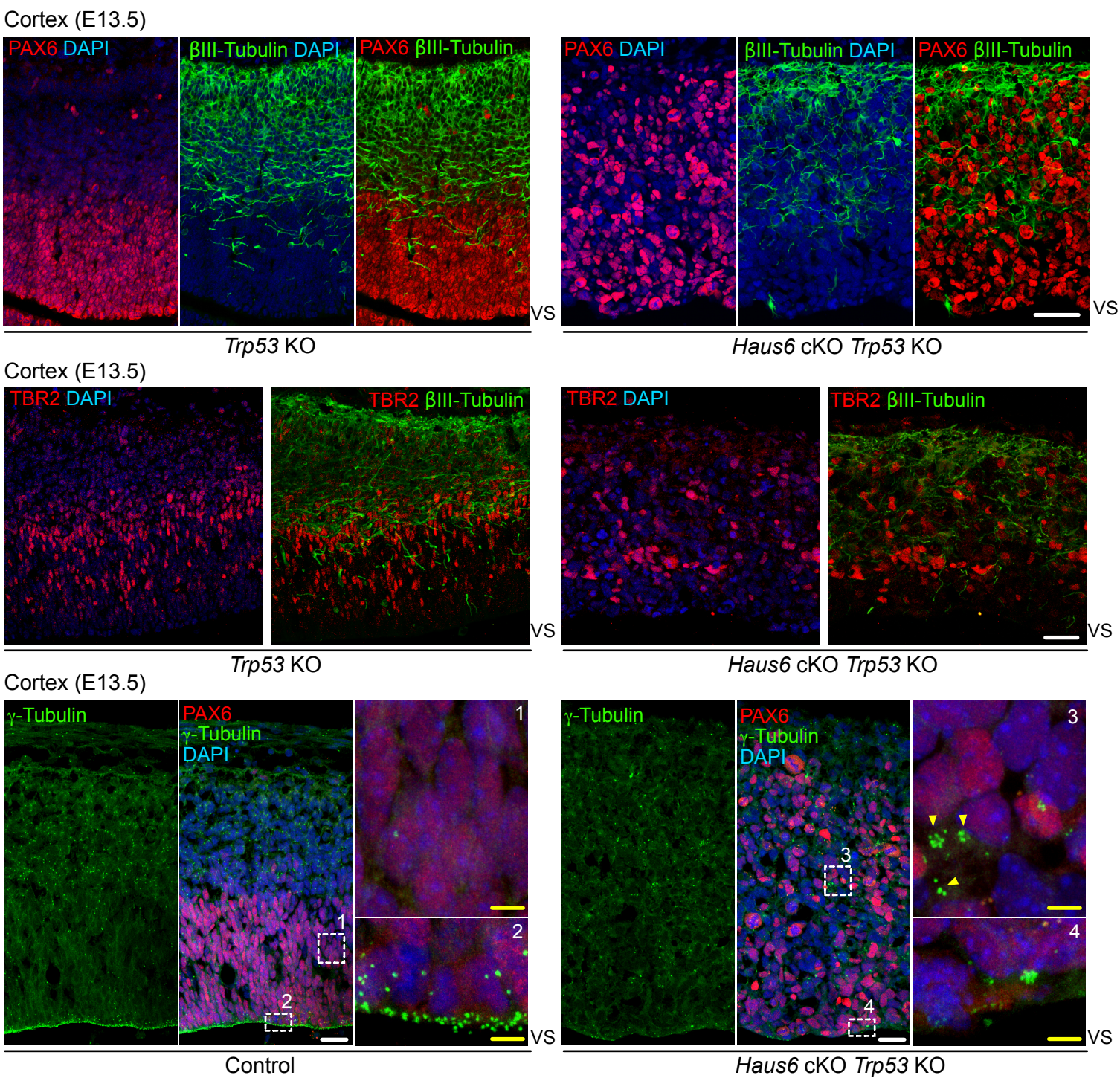
a
Cortex (E13.5)
PAX6 DAPI
βIII-Tubulin DAPI
PAX6 βIII-Tubulin
VS
Trp53 KO
Haus6 cKO Trp53 KO
b
Cortex (E13.5)
TBR2 DAPI
TBR2 βIII-Tubulin
Trp53 KO
Haus6 cKO Trp53 KO
c
Cortex (E13.5)
γ-Tubulin
PAX6
γ-Tubulin
DAPI
Control
Haus6 cKO Trp53 KO

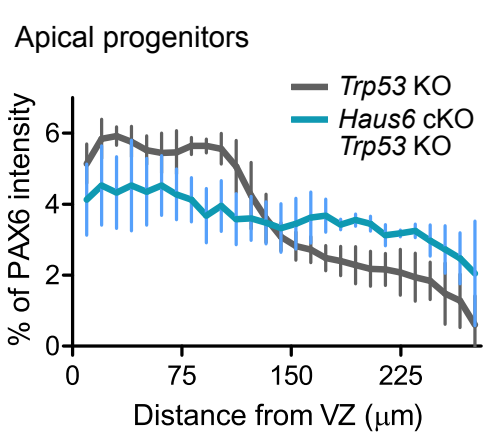
d
Apical progenitors
Trp53 KO
Haus6 cKO
Trp53 KO
% of PAX6 intensity
Distance from VZ (μm)

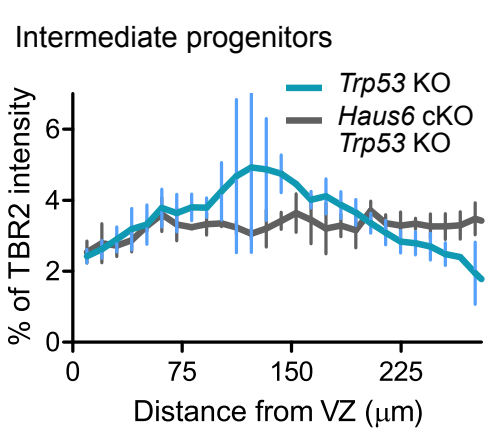
e
Intermediate progenitors
Trp53 KO
Haus6 cKO
Trp53 KO
% of TBR2 intensity
Distance from VZ (μm)

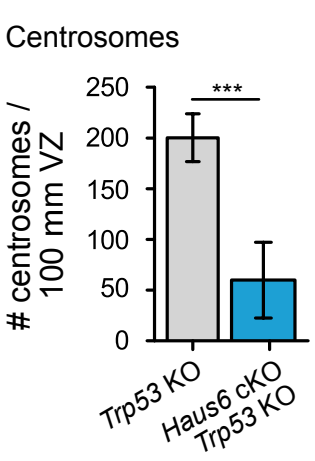
f
Centrosomes
centrosomes / 100 mm VZ
***
Trp53 KO
Haus6 cKO
Trp53 KO

Figure 7-figure supplement 1

a

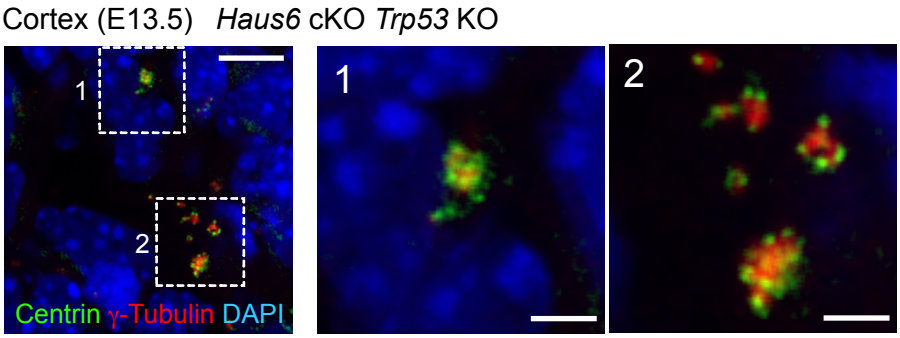

Figure 7-figure supplement 2